



Published in final edited form as:

Cancer Cell. 2020 July 13; 38(1): 97–114.e7. doi:10.1016/j.ccell.2020.04.016.

MAX functions as a tumor suppressor and rewires metabolism in small cell lung cancer

Arnaud Augert¹, Haritha Mathsyaraja², Ali H Ibrahim¹, Brian Freie², Michael J Geuenich^{2,3}, Pei-Feng Cheng², Sydney P Alibeckoff^{1,2}, Nan Wu¹, Joseph B Hiatt¹, Ryan Basom⁴, Adi Gazdar⁵, Lucas B Sullivan^{1,2}, Robert N Eisenman^{2,*}, David MacPherson^{1,6,7,*}

¹Division of Human Biology, Fred Hutchinson Cancer Research Center, 1100 Fairview Ave. N, Seattle, WA 98109, USA

²Basic Sciences Division, Fred Hutchinson Cancer Research Center, Seattle, Washington 98109, USA

³Quest University Canada, 3200 University Blvd, Squamish, BC V8B 0N8, Canada

⁴Genomics and Bioinformatics Shared Resource, Fred Hutchinson Cancer Research Center, 1100 Fairview Ave. N, Seattle, WA 98109, USA

⁵University of Texas, Southwestern, USA. 6000 Harry Hines Blvd. Dallas, TX 75235, USA

⁶Department of Genome Sciences, University of Washington, Seattle, WA 98195, USA

⁷Lead Contact

Summary

Small cell lung cancer (SCLC) is a highly aggressive and lethal neoplasm. To identify candidate tumor suppressors we applied CRISPR-Cas9 gene inactivation screens to a cellular model of early-stage SCLC. Among the top hits was MAX, the obligate heterodimerization partner for MYC family proteins that is mutated in human SCLC. *Max* deletion increases growth and transformation in cells and dramatically accelerates SCLC progression in an *Rb1/Trp53*-deleted mouse model. In contrast, deletion of *Max* abrogates tumorigenesis in MYC-overexpressing SCLC. *Max* deletion in SCLC resulted in de-repression of metabolic genes involved in serine and one carbon metabolism. By increasing serine biosynthesis, *Max* deleted cells exhibit resistance to serine depletion. Thus, *Max* loss results in metabolic rewiring and context-specific tumor suppression.

*Corresponding Authors: eisenman@fredhutch.org; dmacpher@fredhutch.org.

Author Contributions

Conceptualization, A.A.,H.M.,R.N.E.,D.M.; Methodology, A.A.,P.C.,A.I.,B.F.; Software, R.B., B.F.,M.G.; Validation, A.A.,A.I.,H.M.,B.F.,M.G.; Formal analysis, A.A.,R.B.,S.A.,B.F.,M.G.; Investigation, A.A.,S.A.,B.F.,N.W.,A.I.,H.M.,A.G.; Resources, A.A.,L.S.,H.M.,B.F.,P.C.,A.G.,R.N.E.,D.M.; Data Curation, A.A.,R.B.,J.H.,B.F.,M.G.; Writing-Original draft, A.A.,H.M.,R.N.E.,D.M.; Writing-Review & Editing, A.A.,H.M.,B.F.,S.A.,L.S.,R.B.,J.H.,R.N.E.,D.M.; Visualization, A.A., R.B.,H.M.,J.H.,M.G.,B.F.; Supervision, A.A.,L.S.,R.N.E.,D.M.; Project Administration, A.A.,H.M.,R.N.E.,D.M.; Funding Acquisition, R.N.E. and D.M.

Publisher's Disclaimer: This is a PDF file of an unedited manuscript that has been accepted for publication. As a service to our customers we are providing this early version of the manuscript. The manuscript will undergo copyediting, typesetting, and review of the resulting proof before it is published in its final form. Please note that during the production process errors may be discovered which could affect the content, and all legal disclaimers that apply to the journal pertain.

Declaration of Interests

R.N.E is a member of the Scientific Advisory Boards of Kronos Bio Inc. and Shenogen Beijing.

Introduction

Small cell lung cancer (SCLC) is a deadly cancer type with a 5-year survival rate of only 6% (Pietanza et al., 2015). Recent genomic analyses have provided invaluable insights into the etiology of SCLC (Augert et al., 2017; George et al., 2015; Peifer et al., 2012; Rudin et al., 2012). Inactivation of *RB1* and *TP53* tumor suppressor genes and amplification of *MYC* family members, including *MYC*, *MYCL* and *MYCN* are among the most common genetic alterations. Mouse models have validated *MYC* and *MYCL* function as SCLC oncogenes, and *CREBBP* and *PTEN* as tumor suppressors (Cui et al., 2014; Huijbers et al., 2014; Jia et al., 2018; McFadden et al., 2014; Mollaoglu et al., 2017), but the significance of most genomic alterations present in SCLC remains unclear. Genome-wide functional screens have been successfully employed to reveal genes that promote or suppress cell proliferation/viability, and many such genes act in a tissue-specific manner (Sack et al., 2018). Application of functional screens to cellular models of SCLC could help us understand how early-stage lung neuroendocrine cancer cells can become fully transformed, thus revealing genes with tissue-specific tumor suppressor activity in SCLC.

Of relevance to this report is the well-established association of the *MYC* gene family (*MYCL1*, *MYC*, *MYCN*) with SCLC (Peifer et al., 2012; Sos et al., 2012). *MYC* proteins heterodimerize with *MAX* to bind E-Box elements and activate broad programs of gene expression (Diolaiti et al., 2015). *MAX* can also heterodimerize with transcriptional repressors in the *MXD* family (*MXD1-4*, *MNT*) and *MGA* (Carroll et al., 2018). Paradoxically, *MAX* was found to undergo homozygous deletions or mutations in 6/98 SCLC cell lines and tumors (Romero et al., 2014) as well as in other neuroendocrine tumors (Burnichon et al., 2012; Comino-Mendez et al., 2011; Hopewell and Ziff, 1995; Schaefer et al., 2017). To date there is no model system to rigorously examine putative tumor suppressive function of *MAX*. Here we performed functional screens to reveal genes, including *MAX*, with tumor suppressor activity in cellular and in vivo models of SCLC.

Results

Genome-wide CRISPR inactivation screens identify tumor suppressive genes and pathways in SCLC

To identify genes with tumor suppressor activity relevant to SCLC, we employed preSC cells, which are immortal cells derived from early lesions of an *Rb1/Trp53/Rb12*-deleted mouse model of SCLC (Kim et al., 2016). The preSC cellular model exhibits increased proliferation and transformation upon over-expression of oncogenes such as *MYCL* (Kim et al., 2016) and thus represents a sensitized model to identify genes that may functionally contribute to SCLC tumorigenesis. We generated *Trp53*-null mouse embryonic fibroblasts (MEFs) to use in our screens as non-neuroendocrine cell controls. Immunoblots confirmed lack of P53 in the various MEF isolates (Figure S1A). For genome-scale CRISPR-Cas9 screens, we utilized a pooled mouse sgRNA library (Mouse GeCKOv2), comprised of 130,209 sgRNAs targeting a total of 20,611 protein coding genes and 1,175 microRNA precursors (Sanjana et al., 2014). We transduced three replicates each of 250×10^6 cells for both preSCs (n=3) and *Trp53*^{-/-} MEFs (n=3). Viral titers were optimized to result in <30%

transduction rate (MOI<1) and 66x10⁶ transduced cells were maintained throughout the screens in order to preserve a 500X library representation. A reference point (population doubling 0, PD0) for each screen was collected shortly after puromycin selection. Cells were expanded for 12 population doublings after which genomic DNA was extracted, libraries generated, and high throughput sequencing performed (Figure 1A).

Principal component analysis (PCA) revealed preSCs and *Trp53*^{-/-} MEFs clustered similarly at PD0 but displayed cell type specific clustering after expansion for 12 population doublings (Figure 1B). A CRISPR score, defined as the average log₂ fold change in abundance of all sgRNAs targeting a given gene at final versus initial reference (Wang et al., 2015), was computed (Table S1). We also applied MAGeCK VISPR (Li et al., 2015) to identify genes with statistically significant enrichment in our screens considering the performance of all sgRNAs (Table S2). A heatmap shows CRISPR scores for genes with MAGeCK FDR<0.1 that promote preSC growth when inactivated (Figure 1C). These analyses revealed known SCLC tumor suppressor genes such as *Pten* (Cui et al., 2014; McFadden et al., 2014) and also uncovered regulators of early stage SCLC growth. Three major pathways were prominent among enriched “hits” as assessed by MAGeCK VISPR. First, while *PTEN* and *PIK3CA* are frequently affected in SCLC by inactivating and activating mutations, respectively, (Shibata et al., 2009), our screen suggests that other components of the PTEN-PIK3CA-AKT-mTOR pathway also exhibit tumor suppressor function. Indeed, the tumor suppressor genes *Tsc1* and *Tsc2*, which are critical negative regulators of mTORC1, were identified (Figure 1D). Additional negative regulators of mTORC1 signaling were also uncovered including *Sesn3*, *Ddit4* (Brugarolas et al., 2004; Parmigiani et al., 2014) and genes encoding two subunits of GATOR1: *Depdc5* and *Npr13* (Bar-Peled et al., 2013; Panchaud et al., 2013). A second axis identified was the pro-apoptotic pathway including *Bax*, *Bcl2l11* (BIM), *Bbc3* (PUMA) and microRNA genes *miR-15A* and *miR16-1* (Figure 1E). Finally, we identified many members of the stress-activated-protein-kinase pathway (SAPK), including *Map3k12* (DLK), *Map3k13* (MLK), *Map2k4* (MKK4), *Map2k7* (MKK7), *Mapk8* (JNK1) and the downstream transcriptional effector *Jun* (Figure 1F). Genomic position of top hits is plotted in Figure S1B.

Inactivation of members of the PTEN-PIK3CA-AKT-mTOR (Figure 1H), the SAPK (Figure 1I) and the apoptotic (Figure 1J) pathways conferred relative growth advantage in preSCs compared to MEFs as judged by CRISPR scores. Volcano plots show an enrichment for individual guides targeting identified genes in these pathways in preSC cells (Figure S1C–S1E) but not in *Trp53*^{-/-} MEFs, except for *Pten* and *Tsc2* (Figure S1F–S1H). In addition, we also identified genes that are known tumor suppressors previously identified in other cancer types, such as *Tip73*, *Nf1*, *Zhfx3* and *Cdkn1b* (Figure 1G). Among the strongest hits, based on the magnitude of CRISPR score and statistical significance assessed by MAGeCK analyses (Tables S1 and S2) was *Max*, with 5/6 sgRNAs enriched in preSCs after 12 population doublings (Figure S1I). No other members of the MYC network were identified in the screen (Figure S1J). Examination of published genomic data for 110 SCLC patients (predominantly primary SCLC) (George et al., 2015) and data from Project Genie, a tumor mutation database that includes targeted resequencing data for select genes from >400 SCLC patients with primary and metastatic disease (Consortium, 2017), reveals that screen hits *NF1*, *TSC1*, *TSC2*, *PIK3R1*, *DEPDC5*, *TP73*, *CDKN1B*, *ZFH3* and *MAP2K4*

undergo recurrent truncating mutations and deletions in human SCLC (Figure S2A and S2B).

Validation of candidate tumor suppressor genes in SCLC

We next validated a subset of our hits. For 9 genes of interest among the 96 with an FDR <0.1 (MAGeCK analyses) we cloned two guides per gene into the lentiCRISPR_{v2} vector. Following lentiviral infection and selection, gene knockouts were validated by immunoblots (Figure 2A). Expression of sgRNAs targeting *Pten*, *Tsc1*, *Tsc2*, *Map3k12*, *Nf1* and *Max* resulted in increased preSC cell proliferation over an eight-day growth experiment, while sgRNAs targeting *Bcl2l11* and *Bax* did not increase proliferation (Figure 2B). We next assessed gene knockouts for survival at low density and anchorage independent growth. Although *Bcl2l11* and *Bax* KO preSCs did not grow faster than controls, they formed more colonies at low density and showed increased colony forming capability in agar (Figure 2C and 2D). *Map3k12*, *Nf1*, *Max* and PTEN-PIK3CA-AKT-mTOR pathway KOs (*Pten*, *Tsc1* and *Tsc2*) all outgrew controls in both survival at low density and anchorage independent growth (Figure 2C and 2D). These data functionally validate major screen hits as candidate tumor suppressor genes in SCLC, supporting the utility of our experimental approach as a means to assess the importance of genes mutationally inactivated or epigenetically silenced in SCLC.

Max inactivation accelerates SCLC

Max was among the top enriched genes in the screen and we confirmed that *Max* loss increases transformation and produces a pro-proliferative advantage in preSC cells, comparable to deleting the potent SCLC tumor suppressor *Pten* (data not shown). Importantly, in contrast to what we observed in preSCs, *Max* loss did not result in increased growth or survival at low density in *Trp53^{-/-}*, *Trp53^{-/-};sgRb1* or *Trp53^{-/-};sgRb1;sgRb12* MEFs (Figure S3A–S3N). This underscores the cell type-specific effect of MAX loss. *Max* was a particularly intriguing hit owing to a previous report of distinct, inactivating truncating *MAX* mutations in human SCLC (Romero et al., 2014). Thus, to determine whether *Max* functions as an SCLC tumor suppressor gene, we generated an autochthonous SCLC mouse model. We crossed a *Max* floxed allele (Mathsyaraja et al., 2019) into an *Rb1/Trp53*-deleted mouse model of SCLC which develops lung tumors with molecular and histopathological features that resemble human SCLC (Meuwissen et al., 2003).

Two cohorts were infected using intratracheal instillation of Ad-CMV-Cre virus: *Rb1^{lox/lox};Trp53^{lox/lox}* (herein RP) and *Rb1^{lox/lox};Trp53^{lox/lox};Max^{lox/lox}* (herein RPMax) cohorts. We analyzed mice at a fixed 18-week post infection time point and also performed a long-term analysis to assess the impact of *Max* deletion on overall survival (Figure 3A). Magnetic resonance imaging (MRI) and histological analyses revealed a striking increase in lung tumor volume and in the number of lung tumors in the RPMax animals at 18 weeks post Cre delivery (Figure 3B). Long-term analysis revealed that RPMax mice succumbed to lung tumors more rapidly, with a median lung tumor-free survival of 152 days compared to 313 days for the RP control mice (Figure 3C). Histopathology review by a lung cancer pathologist (A.F. Gazdar) confirmed SCLC histology in RP and RPMax models (Figure 3D). A subset of lung tumors that arose from RPMax mice were classified as large

cell neuroendocrine (LNEC) tumors (Figure 3D). Tumors from both groups stained positive for the neuroendocrine marker CGRP (Figure 3E) and immunoblot analysis confirmed loss of MAX protein in the tumors from the RPMax cohort (Figure 3F).

While *Max* inactivation promoted both SCLC and LCNEC, we focused all subsequent molecular and cellular analyses on SCLC, given *MAX* mutations in human SCLC. We used lentiviral transduction of a doxycycline inducible vector to restore MAX expression in a mouse SCLC cell line that we derived from a RPMax lung tumor (herein mRPMax^{KO}). Doxycycline treatment restored MAX expression (Figure 3G) and significantly decreased cell growth (Figure 3H). Of note, doxycycline treatment resulted in approximately 4-fold higher expression relative to MAX-intact mouse SCLCs (Figure 3G). Taken together, these in vivo and cell line data show that *Max* functions as a *bona fide* tumor suppressor gene in SCLC.

MAX is required for MYCL-driven SCLC

The potent tumor suppressor activity of MAX that we observe in vivo is intriguing given that *Myc1* deletion in a mouse SCLC model suppresses tumorigenesis (Kim et al., 2016). These findings raise the question of how MAX acts as a strong tumor suppressor in the same tumor type in which it is presumed to be required by MYCL. It is possible that MYCL could exhibit activities independent of MAX (Steiger et al., 2008; Wert et al., 2001). To rigorously test the impact of MAX loss on tumorigenesis driven by MYCL, we employed a Cre-activated MYCL overexpression allele, herein referred to as *Myc1^{OE}* (Huijbers et al., 2014). With this allele, we can overexpress MYCL in the context of *Max* deletion and compare the kinetics of SCLC emergence across four genotypes: RP; RPMax; *Rb1/Trp53/Myc1^{OE}* (RPMyc1^{OE}) and *Rb1/Trp53/Max/Myc1^{OE}* (RPMaxMyc1^{OE}). Intratracheal instillation of Ad-CGRP-Cre virus, which expresses Cre recombinase under the control of a neuroendocrine-specific *CGRP* promoter (Sutherland et al., 2011) was used to infect the four cohorts. Long-term analysis revealed that RPMax mice became moribund from lung tumors much faster than RP mice, with a median lung tumor-free survival of 259 vs. 601 days ($p < 0.0001$, log-rank test; Figure 4A). Of note, longer latency observed with Ad-CGRP-Cre (Figure 4A) relative to Ad-CMV-Cre (Figure 3C) is consistent with other recent observations (Yang et al., 2018). *Max* deletion or *Myc1* overexpression in neuroendocrine cells using Ad-CGRP-Cre resulted in the development of SCLC tumors with “classic” histology (Figure 4B). The RPMyc1^{OE} cohort exhibited a significant decrease in lung tumor free survival as compared to RP mice and to the RPMax cohort ($p < 0.0001$) (Figure 4A) suggesting greater potency of activating *Myc1* versus inactivating *Max* in driving SCLC tumorigenesis. The RPMaxMyc1^{OE} cohort did not exhibit faster tumorigenesis relative to the RPMyc1^{OE} mice (Figure 4A). Instead, there was a 22-day delay in median survival associated with *Max* deletion, suggesting that MYCL oncogenic function is at least partially suppressed in the absence of MAX. When comparing the RPMaxMyc1^{OE} to the RPMax cohorts, we found faster tumorigenesis in the RPMaxMyc1^{OE} group. While these data raise the possibility that MYCL exhibits MAX-independent oncogenic activity, it was first necessary to determine whether the floxed *Max* alleles were recombined in the tumors that arose. Analyses of tumor derived RNA and protein indicated that 7 of 21 (33%) of RPMaxMyc1^{OE} tumors analyzed escaped homozygous deletion and retained MAX expression (Figure 4C and 4D). PCR

analysis confirmed that tumors with MAX protein expression evident by western blot recombined one but not both alleles of *Max* (Figure S4). These data suggest that tumor cells overexpressing MYCL are under selection to retain MAX. Thus, faster growth of the MYCL-overexpressing MAX positive tumors explains reduced tumor free survival of the R_PMaxMyc1^{OE} compared to the R_PMax groups. Interestingly, the MAX-intact tumors exhibited high MYCL expression but the tumors with MAX loss exhibited low levels of MYCL protein and RNA (Figure 4C and 4D). Thus, lungs from R_PMaxMyc1^{OE} mice exhibit tumors that sustain *Max* deletion and exhibit low MYCL protein and tumors that escape *Max* deletion and support transformation by high MYCL. These data suggest that MYCL-driven and *Max* deletion-driven SCLCs are mutually exclusive transformation events.

To further assess the dependency of MYC family function on MAX we next tested the effect of depleting *Max* in preSCs harboring lentiviral overexpression of MYC, MYCN and MYCL (Figure 4E, 4F and 4G). preSC cell lines overexpressing MYC family members grew faster than their control counterparts (Figure 4H–4J). Upon lentiviral shRNA-mediated *Max* depletion, MYC (Figure 4E), MYCL (Figure 4F) or MYCN (Figure 4G) levels decreased and *Max* depletion abrogated cell growth (Figure 4H–4J). Together, the cellular and in vivo data reveal that MAX does not act as a tumor suppressor in SCLC cells overexpressing MYC family members. We surmise that there is a window in development of SCLC during which *Max* loss and *Rb1/Trp53* deletion cooperate to initiate SCLC tumorigenesis. However, SCLC cells overexpressing *MYC* paralogs are dependent on MAX and represent a distinct evolutionary path of carcinogenesis.

Transcriptional analyses of MAX altered SCLC

We next performed molecular analyses of tissues and cell lines derived from the R_PMax vs R_PAd-CMV-Cre mouse models as well as matched *Max*-WT vs KO preSC cells. MAX can enable transcriptional activation through heterodimerization with MYC members and transcriptional repression through heterodimerization with proteins of the MXD family, MNT and MGA (Diolaiti et al., 2015). To identify genes regulated by MAX in SCLC we performed RNA sequencing (RNA-seq) analyses using the different MAX-perturbed models mentioned above. First, we compared gene expression in RP versus R_PMax mouse SCLC tumors. Second, we compared Max-WT versus Max-KO preSCs. Finally, we restored *Max* expression in the mR_PMax^{KO} mSCLC cell line using an inducible vector (as in Figure 3G) and then examined transcriptional changes. We used EdgeR (Robinson et al., 2010) to identify genes differentially expressed upon either *Max* inactivation or *Max* restoration. An FDR<0.05 cut off revealed 2355 and 3231 differentially expressed genes in mSCLC tumors or preSCs deleted for *Max* respectively (Figure 5A and Figure S5A). A similar cut off applied to *Max* restored mR_PMax^{KO} cells revealed 8055 differentially expressed genes (Figure 5A and Figure S5A). A comparable number of genes were found to be upregulated and downregulated upon MAX alteration in these comparisons (Figure 5A and Figure S5A). We reasoned that key functionally important MAX target genes would be consistently differentially expressed across all three comparisons. Cross model analyses identified a core set of 113 genes, upregulated upon *Max* loss and repressed upon *Max* restoration (Figure 5A). These genes were used as input for enrichment analyses using Enrichr (Kuleshov et al.,

2016). ChIP Enrichment Analysis (ChEA) and Encyclopedia of DNA Elements (ENCODE) analyses for the 113 genes revealed a significant enrichment for MAX and MYC binding sites ($FDR=5.53 \times 10^{-16}$ and $FDR=2.09 \times 10^{-12}$ respectively) (Figure 5B). Also enriched were binding sites for E2F6 and SIN3A ($FDR=3.95 \times 10^{-5}$ and $FDR=1.02 \times 10^{-4}$ respectively) (Figure 5B). E2F6 is a component of an atypical polycomb complex containing MAX and MGA (Gao et al., 2012; Ogawa et al., 2002; Stielow et al., 2018) while MXD-MAX repressive complexes include SIN3A (Ayer et al., 1995; Carroll et al., 2018; Hurlin et al., 1997). In contrast to the data on genes upregulated upon *Max* loss, the same analyses on the core set of 56 genes found downregulated upon *Max* loss and upregulated upon *Max* restoration did not identify significant pathway enrichment (Figure S5A). Overall, our data are consistent with MAX loss primarily causing derepression of genes via MAX- repressive complexes with MXD, MNT or MGA.

Kyoto Encyclopedia of Genes and Genomes (KEGG) analyses of the 113 genes indicated significant enrichment for metabolic pathways, more specifically one carbon pool by folate ($FDR<0.05$) (Figure 5C). The KEGG analyses highlighted the derepression of metabolic genes upon *Max* deletion. Considering that RP tumors were collected at much later time points than R_PMax mSCLC and may have undergone selection for similar changes that *Max* loss induced, we next performed an analysis in which we reduced the stringency of our filters. We identified genes both upregulated upon *Max* deletion in preSCs and downregulated upon *Max* re-expression in the R_PMax^{KO} SCLC cell line. Similar to the 3-model comparison described above, ChEA and ENCODE analyses for the shared 600 genes that changed in the opposite direction compared to MAX (Figure S5B) revealed a significant enrichment for MAX and MYC as well as E2F6 and SIN3A binding sites ($FDR<0.05$) (Figure S5C). KEGG analyses of the same 600 genes identified significant enrichment for the one carbon by folate pathway as well as other metabolic pathways such as alanine, aspartate and glutamate metabolism and amino sugar and nucleotide sugar metabolism ($FDR<0.05$) (Figure S5D). The overlap of the downregulated genes upon *Max* deletion in preSCs and upregulated upon *Max* re-expression in the R_PMax^{KO} SCLC cell line included 770 genes (Figure S5E). ChEA and ENCODE analyses for the shared 770 genes again did not show MYC/MAX binding enrichment (Figure S5F) suggesting MAX functionally drives repression in these systems. Consistent with MAX driving transcriptional repression, meiotic genes *Stag3* and *Meil* known to be repressed by the MAX-associated atypical polycomb complex (Endoh et al., 2017; Suzuki et al., 2016), were strongly activated upon *Max* deletion in the mouse SCLC model and repressed upon *Max* restoration (Figure S5G–I).

Among the metabolic genes up-regulated upon *Max* loss and repressed upon *Max* restoration, we noted several that encode enzymes involved in one carbon metabolism: the serine hydroxymethyltransferase 1 (*Shmt1*), the methylenetetrahydrofolate dehydrogenase (NADP+ dependent) (*Mthfd1*) and the 5-aminoimidazole-4-carboxamide ribonucleotide formyltransferase/IMP cyclohydrolase (*Atic*). We also identified the 3-phosphoglycerate dehydrogenase (*Phgdh*) (Figure 5D–5F), which is the rate limiting enzyme for conversion of glucose into serine, a major fuel for one carbon metabolism. Importantly, enzymes of the one carbon metabolism have been linked to oncogenic properties such as growth, metastasis and survival (Ducker and Rabinowitz, 2017). Upon reexamination of our CRISPR screen data, we found that sgRNAs targeting *Mthfd1*, *Shmt1* and *Phgdh* were preferentially

negatively selected in preSC cells vs MEFs (Figure 5G). Taken together, cross model transcriptional analyses revealed a core set of MAX-regulated genes enriched for metabolic enzymes involved in serine and one carbon metabolism that are functionally important for the growth of preSC cells.

Genomic occupancy studies of MAX in SCLC

We next performed genomic occupancy analyses to identify genes that are direct targets of MAX in both preSCs and upon *Max* restoration in the *Max-null* mRPMAX^{KO} SCLC cell line. As mentioned previously, CHEA analysis on our gene expression data indicated that promoters of genes that are subject to upregulation upon loss of MAX are significantly enriched for repressors such as SIN3A and E2F6. We reasoned that MAX directly represses these genes via heterodimerization with MXD proteins. MNT, one of the most extensively studied MXD proteins, associates with SIN3A and class 1 histone deacetylases, and co-occupies promoters with MAX in several systems, including B lymphocytes, K562 leukemia cells, HepG2 hepatocellular carcinoma cells and 3T3 fibroblasts (ENCODE data, Mathysaraja et al, 2019, unpublished data). We performed ChIP-seq to interrogate MAX, MYC, and MNT occupancy in preSCs. In addition, we also assessed whether increased expression of MAX target genes upon MAX loss corresponds with enhanced association of RNA pol II with these genes. Heat maps showing global analyses of binding revealed a decrease in MAX, MNT and MYC occupancy at the TSS in Max-KO preSCs when compared to controls (Figure 6A, Figure S6A, B). In addition, HOMER analysis of MAX bound motifs revealed a significant enrichment for E-boxes (Figure 6C, Figure S6C). The decrease in MAX and MYC occupancy is consistent with both the loss of heterodimer formation and the strong reduction in their protein levels in *Max-KO* preSCs (Figure S6D). The loss of MNT binding occurs despite an increase in MNT protein levels in Max-KO preSCs (Figure S6D). Importantly, MAX and MNT binding decreased at promoters of genes involved in one carbon metabolism such as *Mthfd1*, *Atic* and *Shmt1*, supporting these genes as direct targets of MAX-mediated repression (Figure 6B, Figure S6E). MYC is also present at these promoters and its binding is also diminished following MAX loss. We frequently observe co-occupancy of MYC, MAX and MXD family proteins at promoters (Figure 6B, Figure S6E) (Mathysaraja et al., 2019 and unpublished data). MAX-MXD heterodimers are generally thought to antagonize MYC function (Carroll et al., 2018; Hurlin et al., 1997; Hurlin et al., 1999), suggesting that such co-occupancy by MAX, MNT, and MYC serves to maintain a balanced transcriptional output that determines tonic expression levels. We hypothesize that MAX loss in SCLC removes this balanced regulation and fuels tumor growth via de-repression of a group of growth-related genes, perhaps mediated by binding of other transcriptional activators. Moreover, when we compared our gene expression and occupancy data, we observed that around 36% of genes upregulated in *Max* KO preSCs are directly bound by MAX in WT preSCs (Figure 6E). The upregulation was accompanied by a significant increase in RNA pol II association with MAX-bound genes in Max-KO preSCs when compared to Max-WT (Figure 6F). This gene activation occurs despite the general decrease in MYC binding at these promoters, further suggesting that MAX-MXD heterodimer activity predominates over or balances MYC-MAX activating heterodimers in the preSC system.

Next, we performed genomic occupancy analyses using CUT& RUN (Janssens et al, 2018) upon restoration of *Max* expression in a R^{PM}Max-deleted mSCLC cell line (mR^{PM}Max^{KO}) using an inducible vector. We observed a strong enrichment for MAX binding in Max-expressing cells when compared to Max-null controls (Figure 6G). This was accompanied by an overall increase of MNT occupancy at the TSS and decrease of RNA pol II occupancy in MAX restored preSCs (Figure 6G–6I). To further confirm the direct binding of repressive heterodimers at key genes, we examined MAX, MNT, MGA and RNA pol II phospho-Ser5 occupancy at key one carbon genes such as *Mthfd1* and *Atic*. We noted a significant increase in MAX, MNT and MGA occupancy in MAX restored cells, suggesting that MAX is capable of directly repressing these genes via heterodimerization with multiple MXD proteins, causing their downregulation in this system (Figure 6H, Figure S6F). Concomitantly, we observed a decrease of RNA pol II phospho-Ser5 binding at these promoters and an overall reduction of Pol II phospho-Ser5 occupancy at genes bound by MAX in MAX restored cells when compared to controls (Figure 6H, I). Overall, these data complement our findings from the preSC system suggesting that MAX predominantly acts as a repressor in the absence of elevated MYC levels. We then overlapped our occupancy data in the MAX restored system with our transcriptional analyses. About 60% of genes that are upregulated or downregulated upon MAX restoration were bound by MAX, indicating that MAX directly regulates a major part of the transcriptional re-wiring that occurs in Max-null SCLC (Figure 6J). Consistent with this idea, we observed enrichment for MAX, MYC, SIN3A and E2F6 and E-boxes when we performed CHEA and HOMER analyses on MAX-bound genes, respectively (Figure 6K, L). Overall, our data strongly suggest that MAX-MXD heterodimers functionally predominate over activating MAX-MYC heterodimers in early stage preSCs. Therefore, loss of MAX leads to the up-regulation of growth promoting genes, such as those involved in one carbon metabolism. Consistent with this, restoration of MAX to a Max-null mSCLC cell line reinstates repression of genes at several thousand loci, including key one carbon metabolic regulators such *Mthfd1*, *Shmt1* and *Atic*. Importantly, several of the 113 genes commonly regulated by MAX in these systems, including *Mthfd1*, *Shmt1* and *Atic* are directly bound by MAX in both preSCs and the MAX restored system (Figure S6G).

Max deletion results in the activation of one carbon and serine biosynthesis metabolic pathways

Our data so far suggests that MAX directly represses many metabolic genes including key regulators of one carbon (1C) metabolism, an observation that may be highly significant in light of recent studies linking upregulation of 1C metabolism to pro-growth phenotypes (Labuschagne et al., 2014; Maddocks et al., 2017). Flux through the 1C pathway can help to meet high demand for nucleic acid production to fuel cancer cell growth. We therefore sought to further elucidate the function of the 1C pathway in SCLC. Immunoblot analyses confirmed upregulation of MTHFD1, SHMT1, ATIC and PHGDH expression upon *Max* loss in preSCs (Figure 7A, 7B). To compare the effects of *Max* loss in preSC cells to that of deleting another SCLC tumor suppressor, *Pten*, which also regulates metabolic targets and increases growth/transformation, we performed western blot analyses for key 1C enzymes. While *Pten* deletion in preSC cells also led to upregulation of PHGDH, upregulation of MTHFD1, ATIC, and SHMT1 was specific to *Max* deletion (Figure S7A). To determine

whether *Max* loss could further enhance the increased proliferation seen with *Pten* loss in the preSC system, we deleted *Max* in *Pten*-null preSC cells. *Max* deletion in *Pten* null preSC cells resulted in increased proliferation that was additive to the effects of *Pten* loss alone (Figure S7B–D).

We next restored MAX in mRPM^{KO} SCLC cells and observed decreases in MTHFD1, SHMT1, ATIC and PHGDH protein levels (Figure 7C, 7D). If upregulation of 1C metabolic processes are important for Max-deleted preSC cells, we reasoned that these cells would exhibit increased sensitivity to methotrexate, a dihydrofolate reductase (DHFR) inhibitor (Farber and Diamond, 1948). Methotrexate acts in part by depleting tetrahydrofolate (THF), an essential co-factor required for folate reactions (Ducker and Rabinowitz, 2017). Indeed, Max-KO preSCs exhibited significantly increased sensitivity to methotrexate compared to preSCs expressing *Max* (Figure 7E). Importantly, this effect was not simply due to augmented growth of the Max-KO preSCs alone, as the increased sensitivity was not observed in *Nfl*-KO preSCs which grow at a similar rate to Max-KO preSC (Figure 7E and data not shown).

Our data also identified PHGDH, which was upregulated following *Max* loss in preSC cells and downregulated following MAX restoration, as a potential MAX target in SCLC cells (Figure 7B, 7D). PHGDH is the first, and rate limiting, enzyme in the de novo serine synthesis pathway from glucose, catalyzing 3-phosphoglycerate into 3-phosphohydroxy-pyruvate. Several cancer types show an upregulation in the expression of the serine synthesis pathway correlated with *PHGDH* amplification or over-expression. PHGDH upregulation leads to increased tumor growth and its depletion abrogates cancer growth (DeNicola et al., 2015; Locasale et al., 2011; Possemato et al., 2011). More recently, PHGDH has been shown to be critical for tumor growth in environments where serine is limiting and is sufficient to promote tumorigenesis in mouse models of cancer (Sullivan et al., 2019). The upregulation of PHGDH upon *Max* deletion led us to hypothesize that *Max* loss would increase the production of serine from glucose. Increased serine production from glucose would also potentially result in increased glycine synthesis through SHMT1, an enzyme that uses THF to convert serine into glycine (Ducker and Rabinowitz, 2017). To test this hypothesis, we set up a time course experiment in which we examined the fate of uniformly ¹³C-labelled glucose (U-¹³C-glucose) in *Max-WT* and *Max-KO* preSCs. As expected, the percentage of carbon labelled serine and glycine increased over time regardless of genotype (Figure 7F). Interestingly, the rate of label incorporation from U-¹³C-glucose into serine and glycine from U-¹³C-glucose increased in *Max-KO* preSCs compared to *Max-WT* preSCs, consistent with increased PHGDH expression (Figure 7F). Isotopologue distribution revealed an increase in serine (M+1-3) and glycine (M+1-2) in Max-KO preSCs (Figure 7F). Notably, partial labeling of serine (M+1 and M+2) also increased in Max-KO preSCs relative to M+3 serine. This finding is consistent with enhanced label scrambling through exchange with glycine by the action of SHMT1, which exhibits increased expression upon *Max* deletion in these cells (Figure 7A). In contrast to the effects of *Max* deletion in preSC cells, MAX restoration in mRPM^{KO} SCLC cells resulted in a decrease in carbon labelling of serine and glycine from U-¹³C-glucose (Figure 7G). U-¹³C glucose derived carbon is incorporated into AMP through ribose production (M+5) and through serine contribution to the purine ring via 10-formyl-tetrahydrofolate (M+1 or M+2) and glycine (M+2). An increase in higher

order labeled species of AMP (M+6-9) from U-¹³C glucose, which require contribution from labeled serine, was observed upon *Max* loss (Figure S7E). Conversely, a significant decrease of AMP labelled carbons (M+6-9) was observed upon MAX restoration (Figure S7F). Collectively, these results suggest increased capacity of *Max*-deficient cells for serine synthesis and one carbon pathway metabolism.

We next tested the capability of MAX altered cells to grow in environments where serine is a limiting factor. We found that *Max-KO* preSCs were strikingly resistant to limiting serine in the media as compared to control preSCs (Figure 7H). Conversely, MAX restoration in the mRPM^{KO} SCLC line re-sensitized cells to loss of viability upon serine depletion (Figure 7I). Taken together, our data demonstrate that *Max* loss upregulates a panel of genes that control serine biosynthesis and one carbon metabolism, with several of these, namely *Atic*, *Mthfdl* and *Shmtl* direct targets of MAX-mediated repression (Figure 6 and Figure S6). Functionally, this enables *Max*-deficient cells to survive and proliferate in the absence of serine. Thus, *Max* loss can lead to growth promoting metabolic rewiring.

Discussion

Applying genome-scale CRISPR-Cas9 screens to a cellular model derived from early-stage mouse SCLC cells, revealed MAX as a candidate tumor suppressor gene in SCLC. Because MAX is an obligate dimerization partner for the entire MYC oncoprotein family, it was paradoxical that MAX loss in preSC cells so dramatically increased cell growth and transformation. Because there is a lack of in vivo evidence validating MAX as a tumor suppressor gene for any tumor type, we deleted *Max* in mouse models sensitized towards developing SCLC. *Max* inactivation cooperated with *Rb1/Trp53* loss to result in dramatic increases in lung tumor size and numbers, a magnitude of effect comparable to deletion of potent tumor suppressors such as *Pten*. Although a previous in vitro study identified genetic MAX inactivation in 6 % of human SCLC cells (Romero et al., 2014) our work provides a rigorous in vivo model to demonstrate tumor suppression conferred by MAX.

Importantly, we observed strong selective pressure to retain *Max* alleles in the context of *Myc1* transgenic overexpression. Our data suggest that the expression/activity of MYC members determines whether MAX loss results in pro or anti-growth phenotypes. In agreement with this hypothesis, we demonstrate that *Max* deletion in preSCs, where MAX-MXD function predominates, leads to increased growth. In contrast, preSCs over-expressing MYC paralogs shifts the stoichiometry towards activating MYC-MAX heterodimers. In this context, we show that the growth of MYC-family overexpressing preSCs was abrogated upon MAX loss. Of note, we performed CRISPR inactivation screens in mouse SCLC cell lines derived from late stage tumors and, unlike our results in preSC cells, have not found enrichment of MAX targeting sgRNAs (unpublished results). We speculate that inactivating mutations in MAX occur at an early stage of SCLC tumor initiation, where MYC paralog activity may be low. Our use of SCLC mouse models and the preSC cellular model allowed targeting of early stage SCLC cells and uncovered the potent context-dependent tumor suppressive activity of MAX. However, once selection for incipient SCLC cells with high expression of MYC/MYCL/MYCN occurs, the pro-proliferative effects of MAX loss are unable to overcome the acute dependence of these cells on MYC function. This notion is

consistent with data showing that *Max* deletion in normal B cells, which express low levels of MYC, has only a modest impact on B cell development in mice (Mathsyaraja et al., 2019; Perez-Olivares et al., 2018). In contrast, in E μ -Myc mice, where high levels of MYC drive lymphomagenesis, loss of MAX completely abrogates lymphoma incidence (Mathsyaraja et al., 2019).

Our analyses reveal repressive MAX-MNT/MXD activity predominates over MYC-MAX in both matched models studied. This is consistent with the significant enrichment we see for SIN3A and E2F6 (part of ncPRC1.6) genomic occupancy at genes upregulated upon *Max* deletion. Loss of MAX-associated repression can have important biological consequences. For example, loss of MAX-MGA re-activates meiotic gene expression programs in embryonic stem and germ cells via displacement of PRC1.6 complexes (Endoh et al., 2017; Suzuki et al., 2016). Indeed, we observed strong activation of meiotic genes upon *Max* deletion in the mouse SCLC model. Moreover, deletion of *Mnt* has been associated with tumorigenesis and disrupted cell cycle control (Hurlin et al., 2003). Across three different transcriptional analyses, the genes upregulated in the absence of MAX were highly enriched for MYC/MAX binding sites, but the downregulated genes exhibited no such enrichment. We hypothesize that tumor promoting activity associated with MAX loss occurs via derepression of key pro-growth genes caused by loss of MAX-MXD/MGA-family heterodimers. The shared MAX bound genes in both models included the one carbon regulators MTHFD1, ATIC and SHMT1. We provide several lines of evidence supporting the notion that regulation of serine and one carbon metabolic enzymes regulated by MAX are functionally important in Max-null SCLC: (i) our CRISPR screen data shows that SHMT1, MTHFD1 and PHGDH are required for preSC growth; (ii) Max-deleted preSC cells exhibit increased sensitivity to folate pathway inhibition using methotrexate; (iii) serine and glycine production from labeled U-¹³C-glucose increased upon MAX loss in preSC cells, while restoration of MAX expression in R^{Max}KO SCLC cells triggered the opposite effects; (iv) we found an increased growth ability for *Max*-null preSCs in serine deprived media and, conversely, sensitization to serine depletion upon reintroduction of MAX in R^{Max}KO SCLC cells. Our data demonstrate that genetic perturbation of MAX alters the expression of multiple metabolic genes in addition to those encoding the one carbon enzymes and consider it likely that many of these also contribute to MAX-dependent tumorigenesis.

Germline MAX mutations in humans are associated with neuroendocrine tumorigenesis beyond SCLC, including the development of pheochromocytomas, paragangliomas and pituitary tumors (Burnichon et al., 2012; Comino-Mendez et al., 2011; Daly et al., 2018). We speculate that a common circuitry among these tumors makes their growth particularly sensitive to activation or suppression of serine/one carbon pathways. In prostate neuroendocrine cancer, for example, a metabolic switch to activate serine and one carbon pathways occurs not with *MAX* deletion but via activation of mTORC1/ATF4 signaling (Reina-Campos et al., 2019). An in-depth analysis of whether de-repression of similar metabolic programs is commonly observed upon MAX inactivation across multiple neuroendocrine tumor types will shed light on why these tumor types undergo selection for *MAX* deletion. The generation of new Max-deleted mouse models for other neuroendocrine

cancer types, including those tumor types that develop in patients with germline mutations in *MAX* will be critical.

Since the discovery of *MAX* nearly three decades ago as the heterodimerization partner required for *MYC* DNA binding (Blackwood and Eisenman, 1991), we have learned a great deal about how *MYC-MAX* promotes tumorigenesis across many cancer types. Recent findings that germline and somatic inactivation mutations in *MAX* result in neuroendocrine cancer types and our own findings that *Max* deletion dramatically promotes SCLC highlight a pressing need to better understand the broader functions of *MAX* beyond interactions with *MYC/MYCN/MYCL*. Our genomic occupancy and gene expression studies reveal that *MAX* and *MNT* repress multiple genes, including those involved in the one carbon pathway, that may contribute to the tumor suppressive function of *MAX*. We expect that *MAX* heterodimers with other *MXD* proteins and/or *MGA* will also mediate repression at other loci involved in growth and proliferation. Recent analyses of TCGA data across many cancer types highlight frequent mutations and deletions in genes encoding *MAX* dimerization partners such as *MNT*, *MGA*, *MXD3* and others (Schaub et al., 2018). *MGA* for example is inactivated in a subset of SCLC (Romero et al., 2014). Surprisingly, *MAX* was the only member of the *MYC* transcription factor network to promote cell growth when deleted in our preSC CRISPR screen. Therefore, simultaneous genetic deletion of multiple *MXD* family proteins may be required to phenocopy the pro-growth effects of *MAX* loss. Our work underscores context dependent functions of *MAX* and how *MAX* heterodimers repress transcription of thousands of genes to mediate tumor suppressive functions in SCLC and in a broad range of malignances.

STAR*METHODS

LEAD CONTACT AND MATERIALS AVAILABILITY

Further information and requests for resources and reagents including plasmids, cell lines and mouse models should be directed to and will be fulfilled by the Lead Contact, David MacPherson (dmacpher@fredhutch.org).

EXPERIMENTAL MODEL AND SUBJECT DETAILS

Animal Studies—We thank Dr. Tyler Jacks for the *Rb1^{lox/lox}* and Dr. Anton Berns for the *Trp53^{lox/lox}* and the *frt-invCAG-Myc11-Luc* strains. We employed either Ad5-CMV-Cre, which expresses Cre under a CMV promoter and cell type specific Ad5-CGRP-Cre, which uses a neuroendocrine-specific promoter to drive Cre expression. Cre expressing adenoviruses were obtained from the University of Iowa Gene Vector Core, with permission of Dr. Anton Berns. The floxed *Max* mice were bred to compound *Rb1^{lox/lox} ; Trp53^{lox/lox}* mice to obtain *Rb1^{lox/lox} ; Trp53^{lox/lox} ; Max* mice. *Rb1^{lox/lox} ; Trp53^{lox/lox} ; Max^{lox/lox}* mice were bred to *Rb1^{lox/lox} ; Trp53^{lox/lox} ; invCAG-Myc11-Luc* to obtain *Rb1^{lox/lox} ; Trp53^{lox/lox} ; Max^{lox/lox} ; invCAG-Myc11-Luc* mice. Genotypes were confirmed by PCR. Littermate controls of indicated genotypes were infected following intratracheal instillation of 3×10^8 plaque-forming units (pfu) of either Ad5-CMV-Cre or Ad5-CGRP-Cre viruses as described (DuPage et al., 2009). Mice were monitored every week following viral infection and euthanized when moribund with labored breathing. Tumor tissues were used to

generate cell lines, frozen for molecular analyses and fixed for histologic analyses as well as immunofluorescence experiments. After excising tumors, the whole lung was inflated with neutral buffered formalin (NBF) and processed for histologic analyses. All animal procedures were approved by the Institutional Animal Care and Use Committee (IACUC) at the Fred Hutchinson Cancer Research Center.

Cell Lines—MEFs were isolated as described above. preSC cell lines were provided by Dr. Kwon Park, isolated as described (Kim et al., 2016). The mRPMa^{KO} cell line was isolated from a *Rb1/Trp53/Max* deleted mouse SCLC tumor. mRPMa^{KO} and preSC(s) were cultured in RPMI 1640 (11875-093, ThermoFisherScientific) supplemented with penicillin (100 U/ml), streptomycin (100 µg/ml) (15140122, ThermoFisherScientific) and 10 % fetal bovine serum (FB-01, Omega Scientific). MEFs were grown in DMEM (11965-092, ThermoFisherScientific) supplemented with penicillin (100 U/ml), streptomycin (100 µg/ml) (15140122, ThermoFisherScientific), and 10 % fetal bovine serum (FB-01, Omega Scientific). Cells were maintained at 37 °C in a humidified atmosphere containing 5 % CO₂ and 95 % air.

METHOD DETAILS

Chemicals—Methotrexate was purchased from Cayman chemical (13960), resuspended according to the manufacturer's recommendations and used at concentrations ranging from 0-100 nM as described in the figure legend. Doxycycline was purchased from Sigma (44577) and used at concentrations ranging from 500-1000 nM as described in figure legends.

Magnetic resonance imaging—Mice from each cohort infected with Ad5-CMV-Cre or Ad5-CGRP-Cre on the same date were monitored by MRI scan (ICON small animal MRI system, Bruker Biospin) to determine lung tumor burden. Mice were anesthetized with isoflurane during imaging. Respiratory gating was employed, and a total of 15 slices of 1 mm thickness was acquired. Tumor volume was quantified using 3D ImageJ Suite with manual quantification of consecutive axial image slices.

Generation of *Trp53*^{flox/flox} MEFs—*Trp53*^{flox/flox} MEFs were generated from embryos at dpc13.5 under a cell culture hood (sterile conditions). Briefly, each embryo was placed in a sterile 10 cm cell culture dish and covered in sterile PBS (1X). Placental and other maternal tissues were removed along with the head and all other innards. The embryo body was moved into a different 10 cm cell culture dish and minced with a sterile razor blade in presence of warm 1 ml trypsin/EDTA (0.05 %) (25300054, ThermoFisherScientific) and incubated for 1 hour at 37 °C. The trypsin was then quenched using DMEM (11965-092, ThermoFisherScientific) and the digested cells mixed and plated into a 10 cm cell culture dish. Cells were briefly cultured (3-4 days), split an additional time to allow for cell expansion and frozen down into multiple vials as early passage stocks. Each embryo was processed separately. In order to inactivate *Trp53*, Cre recombination was performed using Ad5-CMV-Cre viruses (MOI=100) (University of Iowa Gene Vector Core). Two rounds of infections were performed in order to obtain a high recombination rate.

CRISPR–Cas9 based screen—More than 250×10^6 *Trp53*-null MEFs (n=3) and preSCs (n=3) were transduced with the V2 GeCKO mouse library (1000000052, Addgene) at a MOI<1 (30 % transduction rate), puromycin selected for 3-4 days after which 66×10^6 cells, approximately 500X library coverage, were collected (reference point, PD0) and the remaining cells (at least 66×10^6) were seeded, expanded for a total of 12 population doublings (end point, PD12) and collected for subsequent analyses. Genomic DNA extraction, library amplification and high throughput sequencing is described below. Sequencing data was analyzed using MAGeCK-VISPR (Li et al., 2015). Alternatively, CRISPR scores were calculated as described in (Wang et al., 2015). CRISPR scores are defined as the average log₂ fold-change in the final versus initial abundance of all sgRNAs targeting a given gene.

Genomic DNA Extraction—For genomic DNA extraction, a salt precipitation method previously described was used (Chen et al., 2015). In a 15 ml conical tube, 6 ml of NK Lysis Buffer (50 mM Tris, 50 mM EDTA, 1 % SDS, pH 8.0) and 30 μ l of 20 μ g/ml Proteinase K (19131, Qiagen) were added to the cell sample (30×10^6 - 70×10^6 frozen cells) and incubated at 55 °C overnight. The next day, 30 μ l of 10 μ g/ml RNase A (19101, Qiagen) was added to the lysed sample, which was then inverted 25 times and incubated at 37 °C for 30 min. In order to precipitate proteins, samples were cooled on ice before addition of 2 ml of pre-chilled 7.5 M ammonium acetate/dH₂O (A1542, Sigma). Samples were vortexed at high speed and centrifuged at 4,000 g for 10 min at 4 °C. After the spin, a tight pellet was visible in each tube and the supernatant was carefully decanted into a new 15 ml conical tube. Isopropanol (6 ml) was used to precipitate the DNA by inverting 50 times and centrifugation at 4,000 g for 10 min. Genomic DNA pellets were washed with 70 % ethanol and centrifuged at 4,000 g for 5 min. After air-drying the pellets for at least 10 min, the DNA was resuspended in 500 μ l of 1X TE buffer (T9285, Sigma) and incubated at 65 °C for 1 hour and subsequently at room temperature overnight to fully resuspend the DNA. The next day the gDNA was measured using a Nanodrop 2000 (Thermo Fisher Scientific).

V2 GeCKO mouse library propagation and PCR amplification and high throughput sequencing—The V2 GeCKO mouse library was propagated as described in (Sanjana et al., 2014). The sgRNA library readout was performed using a two steps PCR protocol as described in (Chen et al., 2015). The first PCR (12 cycles) was performed to amplify and preserve full library complexity and the second PCR (16-19 cycles) adds appropriate sequencing adapters to the products from the first PCR. To maintain a 500X library representation, 430 μ g of gDNA per condition was PCR amplified. For each 50 μ l reaction, 2 μ g of genomic DNA was used. The second PCR products were migrated on a 2 % agarose gel, pooled and purified using PureLink quick gel extraction kit (K210012, Invitrogen). The purified libraries were quantified using Kapabiosystems Library Quantification Kit (KK4824, Roche) and sequenced on a HiSeq 2500 (Illumina) according to the manufacturer's recommendations. All PCR were performed using Phusion Flash High Fidelity Master Mix (F548L; ThermoFisherScientific) according to the manufacturer's recommendations. PCR primers can be found in (Table S3).

Lentivirus vector production, concentration, and generation of stable lines—

For lentiviral experiments, two sgRNA sequences targeting the genes of interest were selected based on enrichment scores from the whole genome CRISPR screens and cloned into the lentiCRISPR v2 (Addgene plasmid no. 52961) according to the protocol provided by the Zhang Lab. A complete list of CRISPR sequences can be found in (Table S3). Lentiviral vectors were produced by cotransfecting 293TN producer cells (LV900A-1, System Bioscience) with the lentiviral vectors and helper plasmids psPAX2 (Addgene plasmid no. 12260) and pMD2.G (Addgene plasmid no. 12259; ratio, 1:1:0.67) using lipofectamine 2000 (11668019, ThermoFisherScientific) according to the manufacturer's recommendations. Viral supernatants were collected at 48 hours and 72 hours (second collection) after transfection, filtered through a 0.45 µm PVDF syringe filter (F5510, Denville). Viral transductions were performed for 8 hours in the presence of polybrene (4 µg/ml) for preSCs and 16-24 hours in the presence of polybrene (8 µg/ml) for other cell lines. Equal viral titers were used. Puromycin selection (A1113803, ThermoFisherScientific) was performed for 3 to 4 days at 0.8 µg/ml (preSCs), 1 µg/ml (MEFs) and 1.5 µg/ml (mRPMMax^{KO}). preSCs over-expressing MYC members were generated by stable transduction of a lentiviral vector, pLX304 expressing either MYCL, MYC or MYCN. The empty pLX304 vector was used as a control (Addgene plasmid no. 25890). pLX304 expressing either MYCL, MYC or MYCN were generated by Gibson assembly (E5510S, New England Biolabs). Blastidicin (ant-bl-05, Invivogen) selection was performed at 2.5 µg/ml. A MAX inducible lentiviral vector was generated by PCR amplification of the MAX ORF Isoform 2 (NM_145112.2, short isoform) using the Phusion® High-Fidelity PCR Kit (E0553, New England Biolabs) and cloned into the pCW57-RFP-P2A-MCS (Addgene plasmid no. 78933) using EcoR1 and AgeI restriction sites.

RNA extraction and RNA-seq analyses—RNA was extracted using TRIZOL according to the manufacturer's recommendations (15596018, ThermoFisherScientific). Tumor samples were homogenized in TRIZOL using the AgileGrinder™ Tissue Grinder (ACT-AG3080, Thomas Scientific-ACTGene). For RNA-seq analyses, the Ultra RNA Library Prep Kit for Illumina (E7530L, New England BioLabs) was used to generate libraries from total RNA (500 ng). All library preparation was conducted according to the manufacturer's instructions. Single-end sequencing (50 bp) was performed using an Illumina HiSeq 2500, and reads of low quality were filtered before alignment to the mm9 genome build using TopHat v2.0.12 (Trapnell et al., 2009). Cuffdiff v2.1.1 (Trapnell et al., 2013) was used to generate FPKM expression values. Counts were generated from TopHat alignments using the Python package HTSeq v0.6.1 (Anders et al., 2015) using the "intersection-strict" overlap mode. Genes with low counts across conditions were discarded before identification of differentially expressed genes using the Bioconductor package edgeR, v3.16.5 (Robinson et al., 2010). An FDR method (Reiner et al., 2003) was used to correct for multiple testing, where differentially expressed genes were identified with the FDR set at 5 %. Reads from the mRPMMax^{KO} cell line were aligned to the mm9 genome build using STAR v2.5.2a (Dobin et al., 2013) in 2-pass mode, followed by generation of counts for each gene using featureCounts from the Subread package v1.6.0 (Liao et al., 2014).

Genomic Occupancy Studies—For conventional crosslinked ChIP-seq experiments, sgCtrl or sgMax preSC chromatin was used for IP (anti-MYC, MAX, MNT, RNA pol II). Normalization was performed based on protein amounts and ChIP was performed as previously described (Skene and Henikoff, 2015). Libraries were generated using the NEB Ultra II kit. 50X50 paired end sequencing was performed on an Illumina HiSeq 2500 instrument. For CUT&RUN experiments, MAX expression was induced in SCLC tumor lines by doxycycline treatment for 4 days. Cells were bound to ConA beads and permeabilized using a digitonin containing buffer. 1 million cells were used per IP and incubated overnight with antibodies against MYC, MAX and MNT, MGA and RNA polII phosphor Ser-5. The CUT& RUN protocol was followed for library prep (Janssens et al, 2018). Libraries were sequenced using 25x25 paired-end sequencing was performed on an Illumina HiSeq 2500 instrument. 5-10 million reads were obtained per antibody. For both ChIP seq and CUT&RUN experiments, sequences were aligned to the mm10 reference genome assembly using Bowtie2. Spike-in normalization was performed using yeast DNA spike in for CUT&RUN studies whereas library size normalization was done for ChIP-seq experiments. In all cases, peaks were called using MACS at different thresholds. Post peak calling, processing was carried out with bedtools, custom R scripts defining genome position, and the GenomicRanges R package. For MAX, peaks were identified as being associated with a gene if they were within + or – 5 kb from the TSS. For MAX peak calling in preSCs, reads from two independent experiments were aggregated. For CUT&RUN experiments, peak calls from two independent experiments were intersected following IgG subtraction to derive a gene list. For RNA pol II and RNA pol II phosphor-Ser5 peak area, genomic regions +/- 2 kb of the TSS were considered. Genomic plots and heatmaps were made using ngs.plot (Shen et al., 2014) or the R package ggplot2. Heatmaps for genomic binding were made ranking genes according to log fold change in expression from RNA-seq datasets associated with each experiment. Volcano plots were generated using the R package ggplot2. Enrichr was utilized to overlap peak calls with existing ENCODE and ChEA data. De novo and known motif enrichment for sequence specificity was determined using HOMER (Heinz et al., 2010).

Western blot analysis—Whole-cell protein extracts were prepared in cold cell lysis buffer [20 mM Tris-HCl (pH 7.5), 150 mM NaCl, 1 mM Na₂EDTA, 1 mM EGTA, 1 % NP-40, 1 % sodium deoxycholate] supplemented with protease and phosphatase inhibitors (78441, ThermoFisherScientific). Tumor samples were homogenized in cold cell lysis buffer using the AgileGrinder™ Tissue Grinder (ACT-AG3080, Thomas Scientific-ACTGene). Samples were sonicated for 5 minutes, 30 seconds ON/OFF using a Bioruptor (UCD-200, Diagenode). Proteins were quantified using Pierce™ BCA Protein Assay Kit (23227, ThermoFisherScientific), resolved on 4–20 % Mini-PROTEAN®TGX™ Precast Protein Gels (4561096, BioRad), and transferred to Amersham Protran 0.45 NC nitrocellulose membranes (10600002, GE healthcare life science). Protein samples were normalized to ACTB or HSP90. Imaging was performed using the LI-COR Odyssey Fc.

Drug treatments, cell proliferation and viability—Cells were seeded at 7,500 cells per well in 96-well plates and live cell content was estimated using a CellTiter-Glo assay (G7573, Promega) according to the manufacturer's protocol at the times indicated in the

figure legends. Alternatively, for growth in serine deprived media, cells were plated in 12 well plates at 200,000 (preSCs) and 100,000 (mRPM^{Max}^{KO}) and counted using an automated Z2 Series Coulter Counter (6605700, Beckman Coulter). Methotrexate studies were performed in 96-well plates (15,000 cells per well) for 96 hours. CellTiter-Glo was used to determine the relative cell content and viability.

Growth curve analyses—Cells were plated in 6-well plates (200,000 cells/well) on day 0 in the presence or absence of doxycycline (0.5 µg/ml). Doxycycline was replenished every 3 days. The number of cells was counted using an automated Z2 Series Coulter Counter (Beckman Coulter), and the same number of cells was seeded for further counts. Experiments were carried out for a total of 9 days. Population doublings were calculated using the following formula: $n = 3.32 (\log UCY - \log I) + X$, where n is the final population doubling at end of a given subculture, UCY is the cell yield at that point, I is the cell number used as inoculum to begin that subculture, and X is the doubling of the inoculum used to initiate the subculture being quantitated.

Colony formation assays—Cells were seeded at 3×10^3 cells/well (6 well plate), expanded for 2 weeks, fixed with 4 % PFA for 15 minutes and stained with crystal violet solution (0.05 %). The number of colonies per field were counted. Representative wells for each condition are shown.

Anchorage independent growth—Cells (1.5×10^5 /well of a 6 well plate) were seeded in 0.4 % low-melting-point SeaPlaqueTM agarose (Lonza; Catalog no: 50101) on top of 0.8 % low-melting-point SeaPlaqueTM agarose layer. Low-melting-point agarose was premixed with DMEM 2X (Fisher Scientific; SLM202B) complemented with 20 % FBS, sodium pyruvate (2 mmol/L), 200 U/mL penicillin, and 200 µg/mL streptomycin. Cells were allowed to grow at 37 °C with 5 % CO₂ for 3 weeks. For each well, colonies from at least 5 random fields were counted. Representative microscopic images are displayed.

Glucose tracing experiments—Cells were incubated in the presence of Glucose, Glycine and Serine free RPMI (R9660-02, TEKNOVA) supplemented with 10 % dialyzed serum (26400044, ThermoFisherScientific), 10 µg/L Glycine (G5417-100G, Sigma), 30 µg/L L-Serine (S4311-25G, Sigma) and 2 g/L D-Glucose (U-13C6, 99 %) (CLM-1396-PK, Cambridge Isotope Laboratories) for the indicated times. At the time of collection, cells were washed three times in cold saline and the metabolites extracted by scraping the cells in ice cold Methanol (80 %). Chloroform was added and the tubes vortexed at 4 °C for 10 min. The tubes were centrifuged at 4 °C at 16,000 g and the aqueous phase collected. Samples were dried using a speedvac and subsequently ran on the LC-MS.

LC-MS—Metabolite quantitation was performed using a QExactive HF-X Hybrid Quadrupole-Orbitrap Mass Spectrometer equipped with an Ion Max API source and H-ESI II probe, coupled to a Vanquish Flex Binary UHPLC system (Thermo Scientific). Mass calibrations were completed a minimum of once per week using LTQ Velos ESI Calibration Solution (Pierce). Samples were chromatographically separated by injecting a sample volume of 1-3 µL into a SeQuant ZIC-pHILIC Polymeric column (2.1×150 mm 5 µM, EMD Millipore). The flow rate was set to 150 µL/min, autosampler temperature set to 10 °C,

and column temperature set to 30 °C. Mobile Phase A consisted of 20 mM ammonium carbonate and 0.1 % (v/v) ammonium hydroxide, and Mobile Phase B consisted of 100 % acetonitrile. The sample was gradient eluted (%B) from the column as follows: 0-20 min.: linear gradient from 85 % to 20 % B; 20-24 min.: hold at 20 % B; 24-24.5 min.: linear gradient from 20 % to 85 % B; 24.5 min.-end: hold at 85 % B until equilibrated with seven column volumes. Mobile Phase was directed into the ion source with the following parameters: sheath gas = 45, auxiliary gas = 15, sweep gas = 2, spray voltage = 2.9 kV, capillary temperature = 300 °C, RF level = 40 %, auxiliary gas heater temperature = 325 °C. Mass detection was conducted with a resolution of 240,000 in full scan mode or 120,000 in SIM mode, with an AGC target of 3,000,000 and maximum injection time of 100 msec for the full scan mode, or 100,000 and 150 msec for the SIM mode. Metabolites were detected over mass range of 70-1050 m/z in full scan positive mode, or SIM in positive mode using a quadrupole isolation window of 0.7 m/z. Quantitation of metabolites was performed using Tracefinder 4.1 (Thermo Scientific) referencing an in-house metabolite standards library, permitting 5 ppm mass error. Data from stable isotope labeling experiments included a natural abundance correction.

Histology and Immunofluorescence—Mouse lungs were fixed in NBF for 24 hours and then transferred to 70 % ethanol before paraffin embedding. Tissue sections (4 µM thick) were stained with Haemotoxylin and Eosin (H&E). Immunofluorescence was performed on fresh lung tumor tissues fixed in 4% paraformaldehyde (PFA) overnight at 4°C, transferred to 30 % sucrose at 4°C overnight, and then embedded in Tissue-Tek OCT solution and stored at –80 °C. Serial sections (8 µM thick) were cut using a Leica CM1950 cryostat at –20 °C. The following primary antibody was used: anti-CGRP (Rabbit polyclonal; Sigma C8198). Fluorescence images were obtained using a Zeiss LSM 700 confocal microscope. For preserving fluorescence and nuclear counter staining, ProLong Gold Antifade Mountant with DAPI (ThermoFisherScientific, P36935) was used. H&E and immunostained images were acquired using Nikon Eclipse E800 microscope.

Illustration Tool—The graphical abstract image is created with BioRender.

QUANTIFICATION AND STATISTICAL ANALYSIS

GraphPad Prism 7.0 was used to perform statistical analyses. Lung tumor free survival analyses were analyzed using log-rank (Mantel-Cox) test. For the statistical analysis of lung tumor volume (MRI), number of lung tumors, proliferation assays, growth curves, colony formation assays, soft agars experiments and tracing experiments, statistical analyses were performed by Student's unpaired t test. A p value of < 0.05 was considered statistically significant. Error bars represent mean ± SD unless otherwise indicated in the figure legends.

DATA AND CODE AVAILABILITY

The accession number for the raw and processed data of RNA sequencing, CHIP sequencing and CUT&RUN generated and reported in this paper is GEO: GSE138955, GSE146385 and GSE146388.

Supplementary Material

Refer to Web version on PubMed Central for supplementary material.

Acknowledgements

We thank members of the MacPherson, Eisenman, Sullivan and Paddison labs for sharing reagents and providing advice. We would especially like to thank Andrew Snyder, Emily Eastwood, Justin Norton and Eli Grunblatt for their technical help. We thank the Fred Hutch Genomics and Bioinformatics Shared Resource for help regarding the generation and analysis of next generation sequencing data. We also acknowledge support from the Fred Hutch Histopathology and small animal imaging Shared Resources. We are grateful to David Hockenbery for critical reading of the manuscript. These studies were supported in part by NCI R00CA218679 (to LS), NIH/NCI R35CA231989 (to RNE), U01CA235625 and R01CA200547 (to DM) and by NIH/NCI Cancer Center Support Grant P30 CA015704.

REFERENCES

- Amati B, Brooks MW, Levy N, Littlewood TD, Evan GI, and Land H (1993). Oncogenic activity of the c-Myc protein requires dimerization with Max. *Cell* 72, 233–245. [PubMed: 8425220]
- Anders S, Pyl PT, and Huber W (2015). HTSeq—a Python framework to work with high-throughput sequencing data. *Bioinformatics* 31, 166–169. [PubMed: 25260700]
- Augert A, Zhang Q, Bates B, Cui M, Wang X, Wildey G, Dowlati A, and MacPherson D (2017). Small Cell Lung Cancer Exhibits Frequent Inactivating Mutations in the Histone Methyltransferase KMT2D/MLL2: CALGB 151111 (Alliance). *J Thorac Oncol* 12, 704–713. [PubMed: 28007623]
- Ayer DE, Lawrence QA, and Eisenman RN (1995). Mad-Max transcriptional repression is mediated by ternary complex formation with mammalian homologs of yeast repressor Sin3. *Cell* 80, 767–776. [PubMed: 7889570]
- Bar-Peled L, Chantranupong L, Cherniack AD, Chen WW, Ottina KA, Grabiner BC, Spear ED, Carter SL, Meyerson M, and Sabatini DM (2013). A Tumor suppressor complex with GAP activity for the Rag GTPases that signal amino acid sufficiency to mTORC1. *Science* 340, 1100–1106. [PubMed: 23723238]
- Barger CJ, Branick C, Chee L, and Karpf AR (2019). Pan-Cancer Analyses Reveal Genomic Features of FOXM1 Overexpression in Cancer. *Cancers (Basel)* 11.
- Beaulieu ME, Jauset T, Masso-Valles D, Martinez-Martin S, Rahl P, Maltais L, Zacarias-Fluck MF, Casacuberta-Serra S, Serrano Del Pozo E, Fiore C, et al. (2019). Intrinsic cell-penetrating activity propels Omomyc from proof of concept to viable anti-MYC therapy. *Sci Transl Med* 11.
- Berg T, Cohen SB, Desharnais J, Sonderegger C, Maslyar DJ, Goldberg J, Boger DL, and Vogt PK (2002). Small-molecule antagonists of Myc/Max dimerization inhibit Myc-induced transformation of chicken embryo fibroblasts. *Proc Natl Acad Sci U S A* 99, 3830–3835. [PubMed: 11891322]
- Blackwood EM, and Eisenman RN (1991). Max: a helix-loop-helix zipper protein that forms a sequence-specific DNA-binding complex with Myc. *Science* 251, 1211–1217. [PubMed: 2006410]
- Brugarolas J, Lei K, Hurley RL, Manning BD, Reiling JH, Hafen E, Witters LA, Ellisen LW, and Kaelin WG Jr. (2004). Regulation of mTOR function in response to hypoxia by REDD1 and the TSC1/TSC2 tumor suppressor complex. *Genes Dev* 18, 2893–2904. [PubMed: 15545625]
- Burnichon N, Cascon A, Schiavi F, Morales NP, Comino-Mendez I, Abermil N, Inglada-Perez L, de Cubas AA, Amar L, Barontini M, et al. (2012). MAX mutations cause hereditary and sporadic pheochromocytoma and paraganglioma. *Clin Cancer Res* 18, 2828–2837. [PubMed: 22452945]
- Carroll PA, Freie BW, Mathsyaraja H, and Eisenman RN (2018). The MYC transcription factor network: balancing metabolism, proliferation and oncogenesis. *Front Med* 12, 412–425. [PubMed: 30054853]
- Chen S, Sanjana NE, Zheng K, Shalem O, Lee K, Shi X, Scott DA, Song J, Pan JQ, Weissleder R, et al. (2015). Genome-wide CRISPR screen in a mouse model of tumor growth and metastasis. *Cell* 160, 1246–1260. [PubMed: 25748654]

- Comino-Mendez I, Gracia-Aznarez FJ, Schiavi F, Landa I, Leandro-Garcia LJ, Leton R, Honrado E, Ramos-Medina R, Caronia D, Pita G, et al. (2011). Exome sequencing identifies MAX mutations as a cause of hereditary pheochromocytoma. *Nat Genet* 43, 663–667. [PubMed: 21685915]
- Consortium APG (2017). AACR Project GENIE: Powering Precision Medicine through an International Consortium. *Cancer Discov* 7, 818–831. [PubMed: 28572459]
- Cui M, Augert A, Rongione M, Conkrite K, Parazzoli S, Nikitin AY, Ingolia N, and MacPherson D (2014). PTEN is a potent suppressor of small cell lung cancer. *Mol Cancer Res* 12, 654–659. [PubMed: 24482365]
- Daly AF, Castermans E, Oudijk L, Guitelman MA, Beckers P, Potorac I, Neggers S, Sacre N, van der Lely AJ, Bours V, et al. (2018). Pheochromocytomas and pituitary adenomas in three patients with MAX exon deletions. *Endocr Relat Cancer* 25, L37–L42. [PubMed: 29535143]
- DeNicola GM, Chen PH, Mullarky E, Sudderth JA, Hu Z, Wu D, Tang H, Xie Y, Asara JM, Huffman KE, et al. (2015). NRF2 regulates serine biosynthesis in non-small cell lung cancer. *Nat Genet* 47, 1475–1481. [PubMed: 26482881]
- Diolaiti D, McFerrin L, Carroll PA, and Eisenman RN (2015). Functional interactions among members of the MAX and MLX transcriptional network during oncogenesis. *Biochim Biophys Acta* 1849, 484–500. [PubMed: 24857747]
- Dobin A, Davis CA, Schlesinger F, Drenkow J, Zaleski C, Jha S, Batut P, Chaisson M, Gingeras TR (2013). STAR: ultrafast universal RNA-seq aligner. *Bioinformatics*, 29, 15–21. [PubMed: 23104886]
- Ducker GS, and Rabinowitz JD (2017). One-Carbon Metabolism in Health and Disease. *Cell Metab* 25, 27–42. [PubMed: 27641100]
- DuPage M, Dooley AL, and Jacks T (2009). Conditional mouse lung cancer models using adenoviral or lentiviral delivery of Cre recombinase. *Nat Protoc* 4, 1064–1072. [PubMed: 19561589]
- Endoh M, Endo TA, Shinga J, Hayashi K, Farcas A, Ma KW, Ito S, Sharif J, Endoh T, Onaga N, et al. (2017). PCGF6-PRC1 suppresses premature differentiation of mouse embryonic stem cells by regulating germ cell-related genes. *Elife* 6.
- Farber S, and Diamond LK (1948). Temporary remissions in acute leukemia in children produced by folic acid antagonist, 4-aminopteroyl-glutamic acid. *N Engl J Med* 238, 787–793. [PubMed: 18860765]
- Gao Z, Zhang J, Bonasio R, Strino F, Sawai A, Parisi F, Kluger Y, and Reinberg D (2012). PCGF homologs, CBX proteins, and RYBP define functionally distinct PRC1 family complexes. *Mol Cell* 45, 344–356. [PubMed: 22325352]
- George J, Lim JS, Jang SJ, Cun Y, Ozretic L, Kong G, Leenders F, Lu X, Fernandez-Cuesta L, Bosco G, et al. (2015). Comprehensive genomic profiles of small cell lung cancer. *Nature* 524, 47–53. [PubMed: 26168399]
- Heinz S, Benner C, Spann N, Bertolino E, Lin YC, Laslo P, Cheng JX, Murre C, Singh H, and Glass CK (2010). Simple combinations of lineage-determining transcription factors prime cis-regulatory elements required for macrophage and B cell identities. *Mol Cell* 38, 576–589. [PubMed: 20513432]
- Hopewell R, and Ziff EB (1995). The nerve growth factor-responsive PC12 cell line does not express the Myc dimerization partner Max. *Mol Cell Biol* 15, 3470–3478. [PubMed: 7791753]
- Huijbers IJ, Bin Ali R, Pritchard C, Cozijnsen M, Kwon MC, Proost N, Song JY, de Vries H, Badhai J, Sutherland K, et al. (2014). Rapid target gene validation in complex cancer mouse models using re-derived embryonic stem cells. *EMBO Mol Med* 6, 212–225. [PubMed: 24401838]
- Hurlin PJ, Queva C, and Eisenman RN (1997). Mnt, a novel Max-interacting protein is coexpressed with Myc in proliferating cells and mediates repression at Myc binding sites. *Genes Dev* 11, 44–58. [PubMed: 9000049]
- Hurlin PJ, Steingrimsson E, Copeland NG, Jenkins NA, and Eisenman RN (1999). Mga, a dual-specificity transcription factor that interacts with Max and contains a T-domain DNA-binding motif. *EMBO J* 18, 7019–7028. [PubMed: 10601024]
- Hurlin PJ, Zhou ZQ, Toyo-oka K, Ota S, Walker WL, Hirotsune S, and Wynshaw-Boris A (2003). Deletion of Mnt leads to disrupted cell cycle control and tumorigenesis. *EMBO J* 22, 4584–4596. [PubMed: 12970171]

- Janssens DH, Wu SJ, Sarthy JF, Meers MP, Myers CH, Olson JM, Ahmad K, and Henikoff S (2018). Automated in situ chromatin profiling efficiently resolves cell types and gene regulatory programs. *Epigenetics Chromatin* 11, 74. [PubMed: 30577869]
- Jia D, Augert A, Kim DW, Eastwood E, Wu N, Ibrahim AH, Kim KB, Dunn CT, Pillai SPS, Gazdar AF, et al. (2018). Crebbp Loss Drives Small Cell Lung Cancer and Increases Sensitivity to HDAC Inhibition. *Cancer Discov* 8, 1422–1437. [PubMed: 30181244]
- Kim DW, Wu N, Kim YC, Cheng PF, Basom R, Kim D, Dunn CT, Lee AY, Kim K, Lee CS, et al. (2016). Genetic requirement for Myc1 and efficacy of RNA Pol I inhibition in mouse models of small cell lung cancer. *Genes Dev* 30, 1289–1299. [PubMed: 27298335]
- Kuleshov MV, Jones MR, Rouillard AD, Fernandez NF, Duan Q, Wang Z, Koplev S, Jenkins SL, Jagodnik KM, Lachmann A, et al. (2016). Enrichr: a comprehensive gene set enrichment analysis web server 2016 update. *Nucleic Acids Res* 44, W90–97. [PubMed: 27141961]
- Labuschagne CF, van den Broek NJ, Mackay GM, Vousden KH, and Maddocks OD (2014). Serine, but not glycine, supports one-carbon metabolism and proliferation of cancer cells. *Cell Rep* 7, 1248–1258. [PubMed: 24813884]
- Li W, Koster J, Xu H, Chen CH, Xiao T, Liu JS, Brown M, and Liu XS (2015). Quality control, modeling, and visualization of CRISPR screens with MAGeCK-VISPR. *Genome Biol* 16, 281. [PubMed: 26673418]
- Liao Y, Smyth GK and Shi W (2014). featureCounts: an efficient general purpose program for assigning sequence reads to genomic features. *Bioinformatics*, 30(7):923–30. [PubMed: 24227677]
- Locasale JW, Grassian AR, Melman T, Lyssiotis CA, Mattaini KR, Bass AJ, Heffron G, Metallo CM, Muranen T, Sharfi H, et al. (2011). Phosphoglycerate dehydrogenase diverts glycolytic flux and contributes to oncogenesis. *Nat Genet* 43, 869–874. [PubMed: 21804546]
- Maddocks ODK, Athineos D, Cheung EC, Lee P, Zhang T, van den Broek NJF, Mackay GM, Labuschagne CF, Gay D, Kruiswijk F, et al. (2017). Modulating the therapeutic response of tumours to dietary serine and glycine starvation. *Nature* 544, 372–376. [PubMed: 28425994]
- Mathsyaraja H, Freie B, Cheng PF, Babaeva E, Catchpole JT, Janssens D, Henikoff S, and Eisenman RN (2019). Max deletion destabilizes MYC protein and abrogates Emicro-Myc lymphomagenesis. *Genes Dev*.
- McFadden DG, Papagiannakopoulos T, Taylor-Weiner A, Stewart C, Carter SL, Cibulskis K, Bhutkar A, McKenna A, Dooley A, Vernon A, et al. (2014). Genetic and clonal dissection of murine small cell lung carcinoma progression by genome sequencing. *Cell* 156, 1298–1311. [PubMed: 24630729]
- Meuwissen R, Linn SC, Linnoila RI, Zevenhoven J, Mooi WJ, and Berns A (2003). Induction of small cell lung cancer by somatic inactivation of both Trp53 and Rb1 in a conditional mouse model. *Cancer Cell* 4, 181–189. [PubMed: 14522252]
- Metsalu T, and Vilo J (2015). ClustVis: a web tool for visualizing clustering of multivariate data using Principal Component Analysis and heatmap. *Nucleic Acids Res* 43, W566–570. [PubMed: 25969447]
- Mollaoglu G, Guthrie MR, Bohm S, Bragelmann J, Can I, Ballieu PM, Marx A, George J, Heinen C, Chalishazar MD, et al. (2017). MYC Drives Progression of Small Cell Lung Cancer to a Variant Neuroendocrine Subtype with Vulnerability to Aurora Kinase Inhibition. *Cancer Cell* 31, 270–285. [PubMed: 28089889]
- Ogawa H, Ishiguro K, Gaubatz S, Livingston DM, and Nakatani Y (2002). A complex with chromatin modifiers that occupies E2F- and Myc-responsive genes in G0 cells. *Science* 296, 1132–1136. [PubMed: 12004135]
- Panchaud N, Peli-Gulli MP, and De Virgilio C (2013). Amino acid deprivation inhibits TORC1 through a GTPase-activating protein complex for the Rag family GTPase Gtr1. *Sci Signal* 6, ra42. [PubMed: 23716719]
- Parmigiani A, Nourbakhsh A, Ding B, Wang W, Kim YC, Akopiants K, Guan KL, Karin M, and Budanov AV (2014). Sestrins inhibit mTORC1 kinase activation through the GATOR complex. *Cell Rep* 9, 1281–1291. [PubMed: 25457612]

- Peifer M, Fernandez-Cuesta L, Sos ML, George J, Seidel D, Kasper LH, Plenker D, Leenders F, Sun R, Zander T, et al. (2012). Integrative genome analyses identify key somatic driver mutations of small-cell lung cancer. *Nat Genet* 44, 1104–1110. [PubMed: 22941188]
- Perez-Olivares M, Trento A, Rodriguez-Acebes S, Gonzalez-Acosta D, Fernandez-Antoran D, Roman-Garcia S, Martinez D, Lopez-Briones T, Torroja C, Carrasco YR, et al. (2018). Functional interplay between c-Myc and Max in B lymphocyte differentiation. *EMBO Rep* 19.
- Pietanza MC, Byers LA, Minna JD, and Rudin CM (2015). Small cell lung cancer: will recent progress lead to improved outcomes? *Clin Cancer Res* 21, 2244–2255. [PubMed: 25979931]
- Possemato R, Marks KM, Shaul YD, Pacold ME, Kim D, Birsoy K, Sethumadhavan S, Woo HK, Jang HG, Jha AK, et al. (2011). Functional genomics reveal that the serine synthesis pathway is essential in breast cancer. *Nature* 476, 346–350. [PubMed: 21760589]
- Reina-Campos M, Linares JF, Duran A, Cordes T, L'Hermitte A, Badur MG, Bhangoo MS, Thorson PK, Richards A, Rooslid T, et al. (2019). Increased Serine and One-Carbon Pathway Metabolism by PKC*lambda*/iota Deficiency Promotes Neuroendocrine Prostate Cancer. *Cancer Cell* 35, 385–400 e389. [PubMed: 30827887]
- Reiner A, Yekutieli D, and Benjamini Y (2003). Identifying differentially expressed genes using false discovery rate controlling procedures. *Bioinformatics* 19, 368–375. [PubMed: 12584122]
- Robinson MD, McCarthy DJ, and Smyth GK (2010). edgeR: a Bioconductor package for differential expression analysis of digital gene expression data. *Bioinformatics* 26, 139–140. [PubMed: 19910308]
- Romero OA, Torres-Diz M, Pros E, Savola S, Gomez A, Moran S, Saez C, Iwakawa R, Villanueva A, Montuenga LM, et al. (2014). MAX inactivation in small cell lung cancer disrupts MYC-SWI/SNF programs and is synthetic lethal with BRG1. *Cancer Discov* 4, 292–303. [PubMed: 24362264]
- Rudin CM, Durinck S, Stawiski EW, Poirier JT, Modrusan Z, Shames DS, Bergbower EA, Guan Y, Shin J, Guillory J, et al. (2012). Comprehensive genomic analysis identifies SOX2 as a frequently amplified gene in small-cell lung cancer. *Nat Genet* 44, 1111–1116. [PubMed: 22941189]
- Sack LM, Davoli T, Li MZ, Li Y, Xu Q, Naxerova K, Wooten EC, Bernardi RJ, Martin TD, Chen T, et al. (2018). Profound Tissue Specificity in Proliferation Control Underlies Cancer Drivers and Aneuploidy Patterns. *Cell* 173, 499–514 e423. [PubMed: 29576454]
- Sage J, Miller AL, Perez-Mancera PA, Wysocki JM, and Jacks T (2003). Acute mutation of retinoblastoma gene function is sufficient for cell cycle re-entry. *Nature* 424, 223–228. [PubMed: 12853964]
- Sanjana NE, Shalem O, and Zhang F (2014). Improved vectors and genome-wide libraries for CRISPR screening. *Nat Methods* 11, 783–784. [PubMed: 25075903]
- Schaefer IM, Wang Y, Liang CW, Bahri N, Quattrone A, Doyle L, Marino-Enriquez A, Lauria A, Zhu M, Debiec-Rychter M, et al. (2017). MAX inactivation is an early event in GIST development that regulates p16 and cell proliferation. *Nat Commun* 8, 14674. [PubMed: 28270683]
- Schaub FX, Dhankani V, Berger AC, Trivedi M, Richardson AB, Shaw R, Zhao W, Zhang X, Ventura A, Liu Y, et al. (2018). Pan-cancer Alterations of the MYC Oncogene and Its Proximal Network across the Cancer Genome Atlas. *Cell Syst* 6, 282–300 e282. [PubMed: 29596783]
- Shen L, Shao N, Liu X, and Nestler E (2014). ngs.plot: Quick mining and visualization of next-generation sequencing data by integrating genomic databases. *BMC Genomics* 15, 284. [PubMed: 24735413]
- Shen-Li H, O'Hagan RC, Hou H Jr., Horner JW 2nd, Lee HW, and DePinho RA (2000). Essential role for Max in early embryonic growth and development. *Genes Dev* 14, 17–22. [PubMed: 10640271]
- Shibata T, Kokubu A, Tsuta K, and Hirohashi S (2009). Oncogenic mutation of PIK3CA in small cell lung carcinoma: a potential therapeutic target pathway for chemotherapy-resistant lung cancer. *Cancer Lett* 283, 203–211. [PubMed: 19394761]
- Skene PJ, and Henikoff S (2015). A simple method for generating high-resolution maps of genome-wide protein binding. *Elife* 4, e09225. [PubMed: 26079792]
- Sos ML, Dietlein F, Peifer M, Schottle J, Balke-Want H, Muller C, Koker M, Richters A, Heynck S, Malchers F, et al. (2012). A framework for identification of actionable cancer genome dependencies in small cell lung cancer. *Proc Natl Acad Sci U S A* 109, 17034–17039. [PubMed: 23035247]

- Steiger D, Furrer M, Schwinkendorf D, and Gallant P (2008). Max-independent functions of Myc in *Drosophila melanogaster*. *Nat Genet* 40, 1084–1091. [PubMed: 19165923]
- Stielow B, Finkernagel F, Stiewe T, Nist A, and Suske G (2018). MGA, L3MBTL2 and E2F6 determine genomic binding of the non-canonical Polycomb repressive complex PRC1.6. *PLoS Genet* 14, e1007193. [PubMed: 29381691]
- Struntz NB, Chen A, Deutzmann A, Wilson RM, Stefan E, Evans HL, Ramirez MA, Liang T, Caballero F, Wildschut MHE, et al. (2019). Stabilization of the Max Homodimer with a Small Molecule Attenuates Myc-Driven Transcription. *Cell Chem Biol* 26, 711–723 e714. [PubMed: 30880155]
- Sullivan MR, Mattaini KR, Dennstedt EA, Nguyen AA, Sivanand S, Reilly MF, Meeth K, Muir A, Darnell AM, Bosenberg MW, et al. (2019). Increased Serine Synthesis Provides an Advantage for Tumors Arising in Tissues Where Serine Levels Are Limiting. *Cell Metab* 29, 1410–1421 e1414. [PubMed: 30905671]
- Sutherland KD, Proost N, Brouns I, Adriaensen D, Song JY, and Berns A (2011). Cell of origin of small cell lung cancer: inactivation of Trp53 and Rb1 in distinct cell types of adult mouse lung. *Cancer Cell* 19, 754–764. [PubMed: 21665149]
- Suzuki A, Hirasaki M, Hishida T, Wu J, Okamura D, Ueda A, Nishimoto M, Nakachi Y, Mizuno Y, Okazaki Y, et al. (2016). Loss of MAX results in meiotic entry in mouse embryonic and germline stem cells. *Nat Commun* 7, 11056. [PubMed: 27025988]
- Trapnell C, Hendrickson DG, Sauvageau M, Goff L, Rinn JL, and Pachter L (2013). Differential analysis of gene regulation at transcript resolution with RNA-seq. *Nat Biotechnol* 31, 46–53. [PubMed: 23222703]
- Trapnell C, Pachter L, and Salzberg SL (2009). TopHat: discovering splice junctions with RNA-Seq. *Bioinformatics* 25, 1105–1111. [PubMed: 19289445]
- Wang T, Birsoy K, Hughes NW, Krupczak KM, Post Y, Wei JJ, Lander ES, and Sabatini DM (2015). Identification and characterization of essential genes in the human genome. *Science* 350, 1096–1101. [PubMed: 26472758]
- Wert M, Kennedy S, Palfrey HC, and Hay N (2001). Myc drives apoptosis in PC12 cells in the absence of Max. *Oncogene* 20, 3746–3750. [PubMed: 11439337]
- Yang D, Denny SK, Greenside PG, Chaikovskiy AC, Brady JJ, Ouadah Y, Granja JM, Jahchan NS, Lim JS, Kwok S, et al. (2018). Intertumoral Heterogeneity in SCLC Is Influenced by the Cell Type of Origin. *Cancer Discov* 8, 1316–1331. [PubMed: 30228179]
- Yang X, Boehm JS, Yang X, Salehi-Ashtiani K, Hao T, Shen Y, Lubonja R, Thomas SR, Alkan O, Bhimdi T, et al. (2011). A public genome-scale lentiviral expression library of human ORFs. *Nat Methods* 8, 659–661. [PubMed: 21706014]
- Yin C, Knudson CM, Korsmeyer SJ, and Van Dyke T (1997). Bax suppresses tumorigenesis and stimulates apoptosis in vivo. *Nature* 385, 637–640. [PubMed: 9024662]

Highlights

- CRISPR-Cas9 screens identify candidate tumor suppressor genes and pathways in SCLC
- MAX is a context-dependent tumor suppressor in early stage SCLC
- MAX is required for MYC-driven SCLC and MAX tumor suppression is independent of MYC
- MAX represses metabolic genes including regulators of one carbon metabolism

Highlights

Augert et al. identify MAX as a context-dependent tumor suppressor in small cell lung cancer (SCLC) that can regulate serine and one carbon metabolism. MAX loss accelerates SCLC progression in a *Rb1/Tip53*-deficient mouse model, while abrogating tumorigenesis in MYCL-overexpressing SCLC.

Significance

MAX is an obligate heterodimerization partner for MYC oncoproteins. Genomic binding and transformation activities driven by dysregulated MYC in many cancers are known to require MAX. SCLC, a neuroendocrine tumor type, frequently exhibits amplification of *MYC* family genes. Paradoxically however, a subset of human SCLC exhibits deletions or inactivating mutations in *MAX*, and germline inactivating mutations in *MAX* predisposes to other neuroendocrine cancers. Here we have developed both cell-based and murine models demonstrating accelerated SCLC progression upon inactivation of *Max*. We show that widespread gene expression changes and metabolic alterations in cells transformed by *Max* loss are independent of MYC and that MYC overexpression is unable to transform *Max*-null cells. Therefore, *MAX* inactivation constitutes a MYC-independent pathway to SCLC.

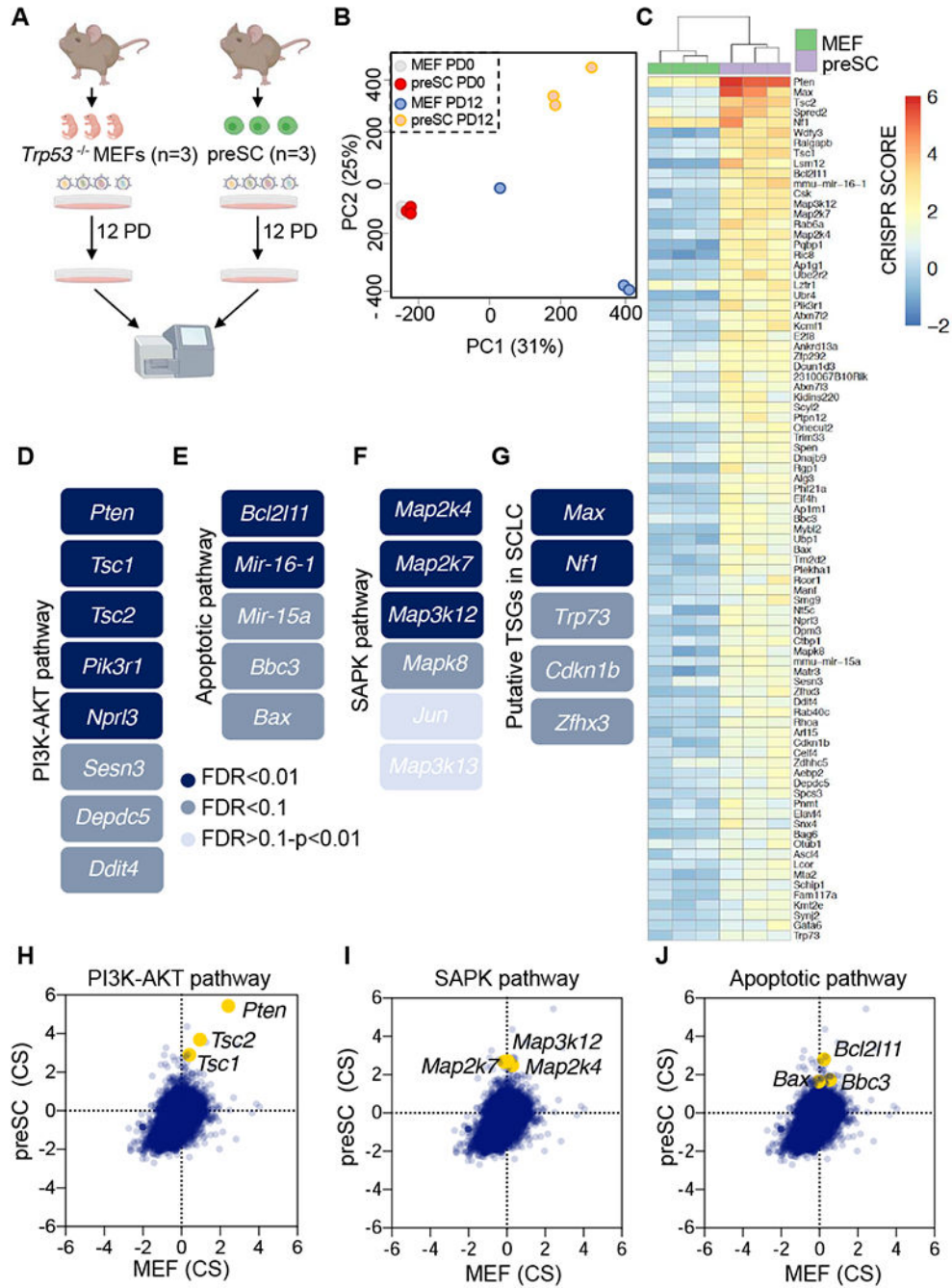


Figure 1. A whole genome CRISPR screen identifies candidate SCLC tumor suppressor genes and pathways
A, Schematic of CRISPR screening strategy. **B**, Principal component analysis (PCA) of the individual libraries generated from each replicate (PD0 and PD12) for MEFs and preSCs. **C**, Heat map of the top screen hits (MAGeCK FDR<0.1) enriched in preSCs as compared to MEFs. CRISPR scores are shown. **D-G**, Schematic of the PI3K-AKT pathway (**D**), the apoptotic pathway (**E**), the SAPK pathway (**F**) and putative tumor suppressor genes (**G**) identified in preSCs. FDR values are indicated and color coded. **H-J**, Scatter plot using

CRISPR scores for the selected genes in the PI3K-AKT pathway (**H**), SAPK pathway (**I**) and the apoptotic pathway (**J**). For **D-G**, FDR values were calculated using MAGeCK VISPR. See also Figures S1 and S2 and Tables S1 and S2.

Author Manuscript

Author Manuscript

Author Manuscript

Author Manuscript

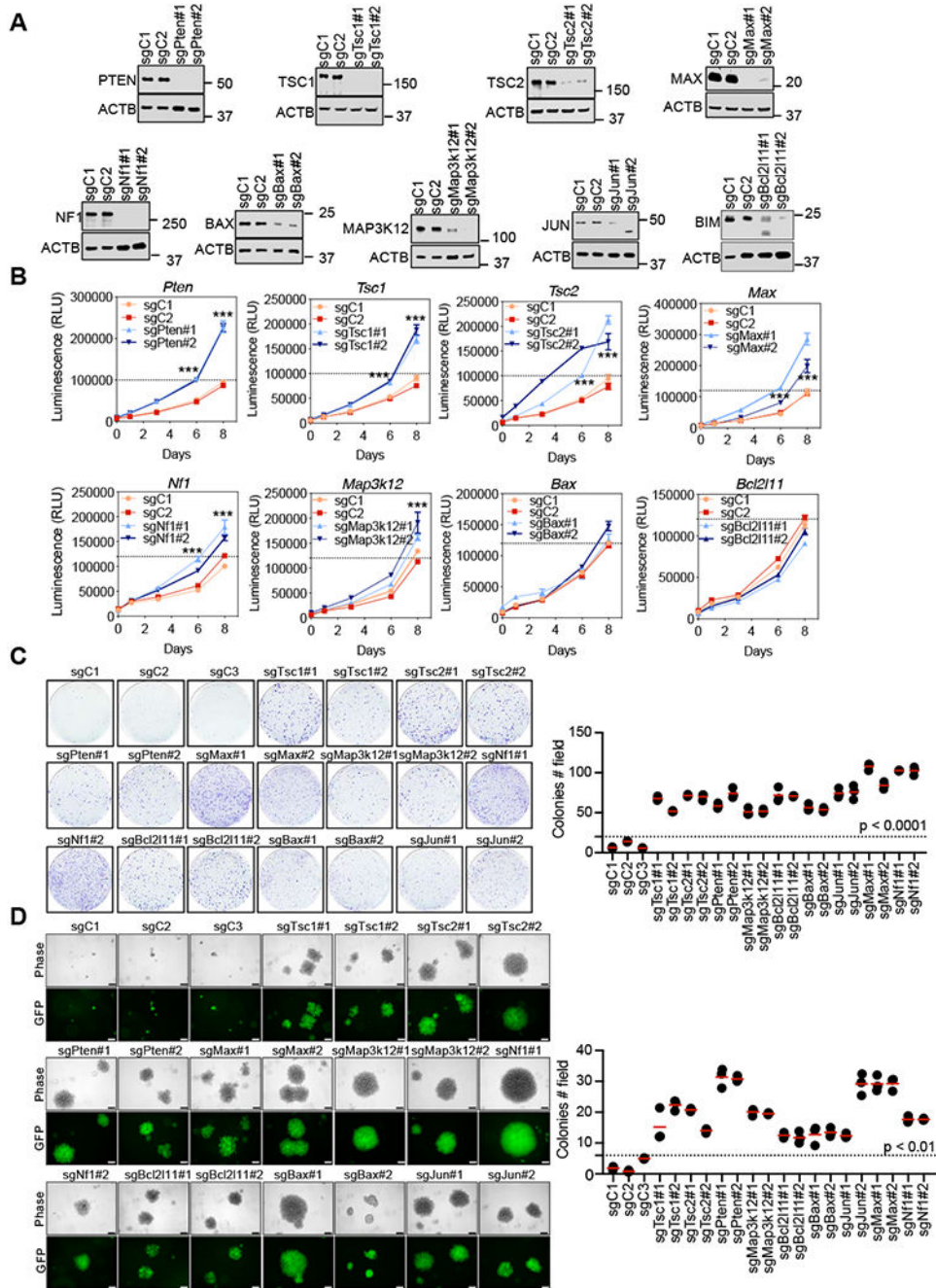


Figure 2. Validation of candidate tumor suppressor genes in SCLC

A, Immunoblotting results following lentiviral sgRNA expression for the indicated genes in preSCs. ACTB was used as a loading control. **B**, CellTiter-Glo viability assay for the indicated genes. Two sgRNAs were used for each gene. Representative experiments from at least 2 independent experiments are shown. Error bars represent mean ± SD (n=3) ***p<.001, unpaired Student’s t test. RLU, relative luminescence units. **C**, Colony formation assays by crystal violet staining after 2 weeks expansion of cells (6 well plates) were performed for the indicated genes. The number of colonies per field were counted.

Error bars represent the mean (n= 3 independent experiments), $p < 0.0001$, unpaired Student's t test. **D**, Anchorage-independent assay upon the inactivation for the genes of interest in soft agar. n = 3 independent experiments. Error bars represent mean \pm SD, $p < 0.01$, unpaired Student's t test. Scale bar: 100 μ M.

Author Manuscript

Author Manuscript

Author Manuscript

Author Manuscript

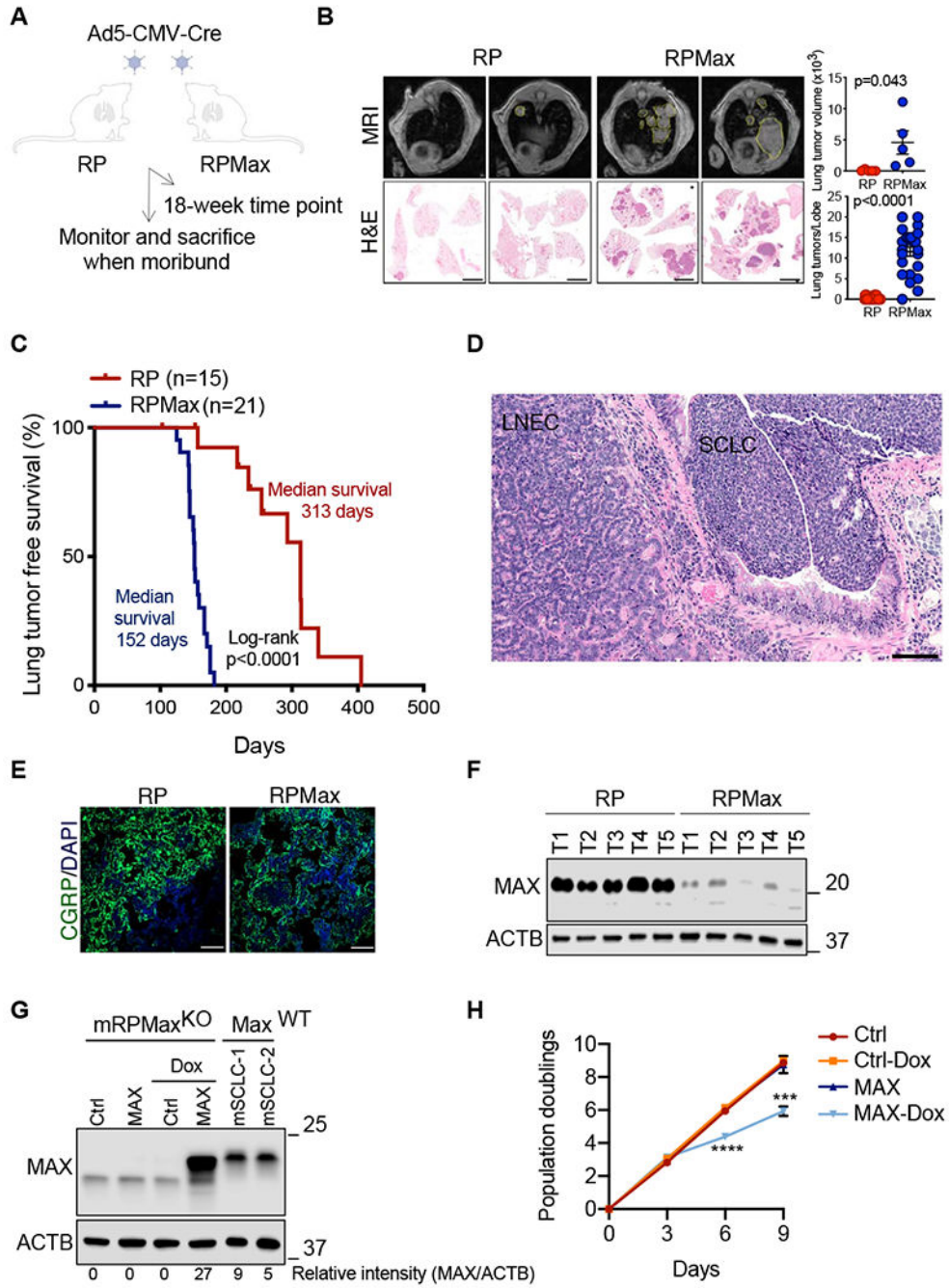


Figure 3. Max inactivation accelerates SCLC

A, Schematic of the strategy to follow effects of *Max* deletion in a mouse model of SCLC. **B**, Magnetic resonance imaging (MRI) and Hematoxylin and Eosin (H&E) stains for the indicated genotypes 18 weeks post Ad5-CMV-Cre infections. Representative images of mice are shown. Error bars represent mean \pm SD (n=5 mice per genotype). Unpaired Student's t test was performed and p values are shown. Scale bar: 2 mm. **C**, Kaplan-Meier tumor-free survival curves of *Rb1/Trp53* mutant (red, n=15) and *Rb1/Trp53/Max* mutant (blue, n=21) mice from autochthonous model infected with Ad5-CMV-Cre (Day 0). Statistical

significance for the overall survival of the cohorts was calculated using log-rank (Mantel-Cox) test. **D**, Representative H&E stained section of SCLC and LNEC from the *Rb1/Trp53/Max* cohort. Scale bar: 100 μ m. **E**, Representative immunofluorescence for the SCLC marker CGRP in each cohort (*Rb1/Trp53* vs. *Rb1/Trp53/Max*). DAPI was used as a nuclear stain. Scale bar: 50 μ m. **F**, Representative immunoblotting results of MAX protein levels in 5 lung tumor tissues from each cohort (*Rb1/Trp53* vs. *Rb1/Trp53/Max*). ACTB was used as a loading control. **G**, Representative immunoblotting of MAX protein levels upon doxycycline-inducible *Max* restoration in a mRPM^{KO} (*Rb1/Trp53/Max*-deleted) mSCLC cell line. ACTB was used as a loading control and two RP mSCLCs expressing endogenous MAX levels were used as internal controls. Protein levels were quantified using the LI-COR software. **H**, Growth curve analysis of a mRPM^{KO} cells upon *Max* restoration at the indicated times following doxycycline addition. Error bars represent mean \pm SD (n=3 independent experiments). ***, p<0.005; ****, p<0.0001, unpaired Student's t test. See also Figure S3.

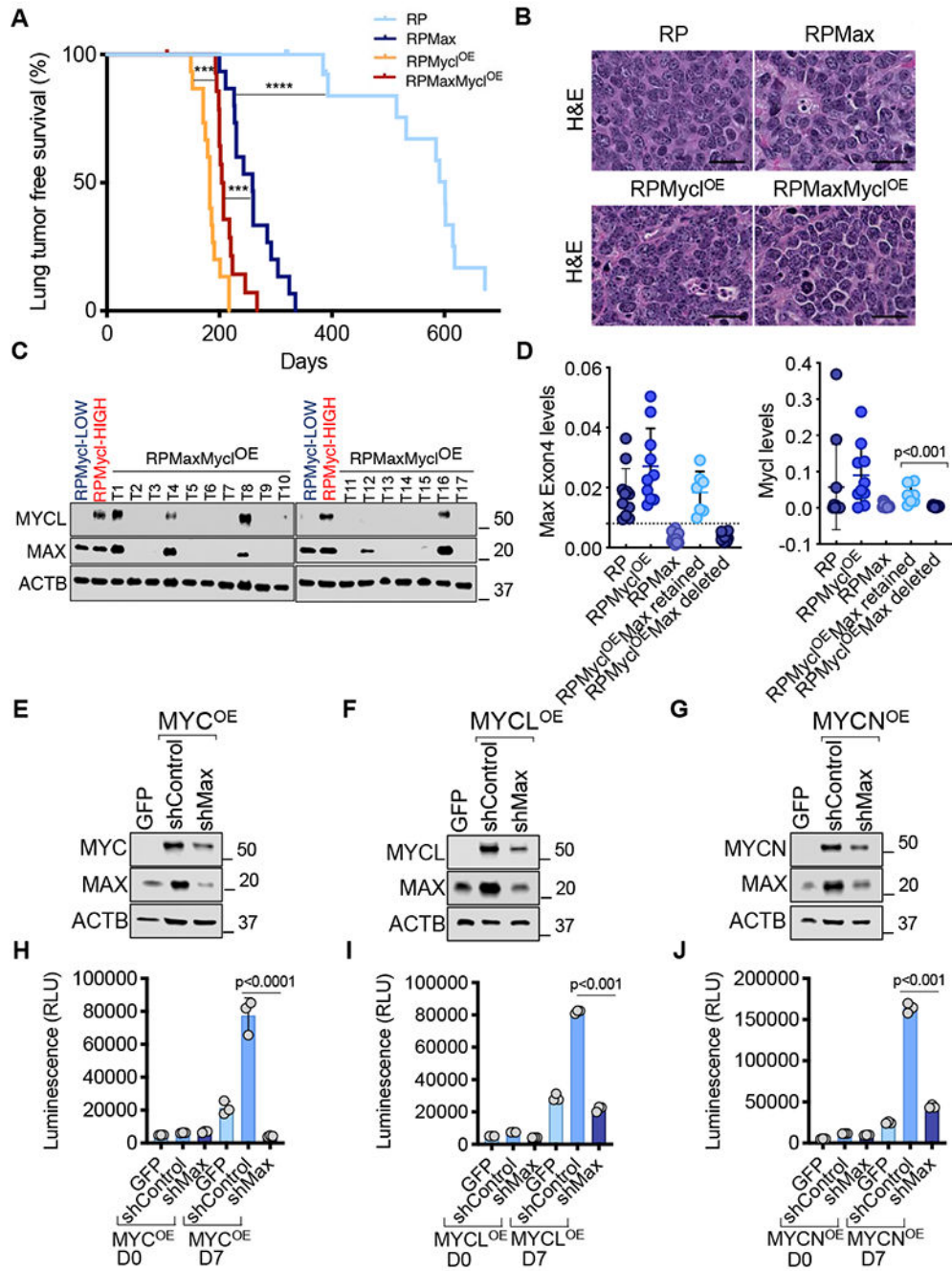


Figure 4. MAX is required for SCLC that is driven by MYC family members
A, Kaplan-Meier tumor-free survival of RP (n=15), RPMax (n=15), RPMyc1^{OE} (n=15) and RPMaxMyc1^{OE} cohorts (n=15) from autochthonous model infected with Ad-CGRP-Cre (Day 0). Statistical significance for the overall survival of the different cohorts was calculated using log-rank (Mantel-Cox) test. ***, p<0.001; ****p<0.0001. **B**, Representative H&E stained section of SCLC for the indicated cohorts. Scale bar: 50 μM. **C**, Immunoblotting of MYC and MAX protein levels. ACTB was used as a loading control. **D**, Quantitative PCR analyses of *Max* (Exon 4) and *Mycl* levels relative to *Gapdh* as a loading

control. Error bars represent mean \pm SD (n = 7 tumors per group). Unpaired Student's t test was used. **E-G**, Immunoblotting of MYC (**E**), MYCL (**F**), MYCN (**G**) and MAX protein levels upon *Max* knockdown in MYC (**E**), MYCL (**F**) and MYCN (**G**) over-expressing preSCs. ACTB was used as a loading control. **H-J**, CellTiter-Glo viability assay upon *Max* knockdown in MYC (**H**), MYCL (**I**) and MYCN (**J**) overexpressing preSCs. Error bars represent mean \pm SD (n=3 independent experiments); p values are indicated, unpaired Student's t test. RLU, relative luminescence units. See also Figure S4.

Author Manuscript

Author Manuscript

Author Manuscript

Author Manuscript

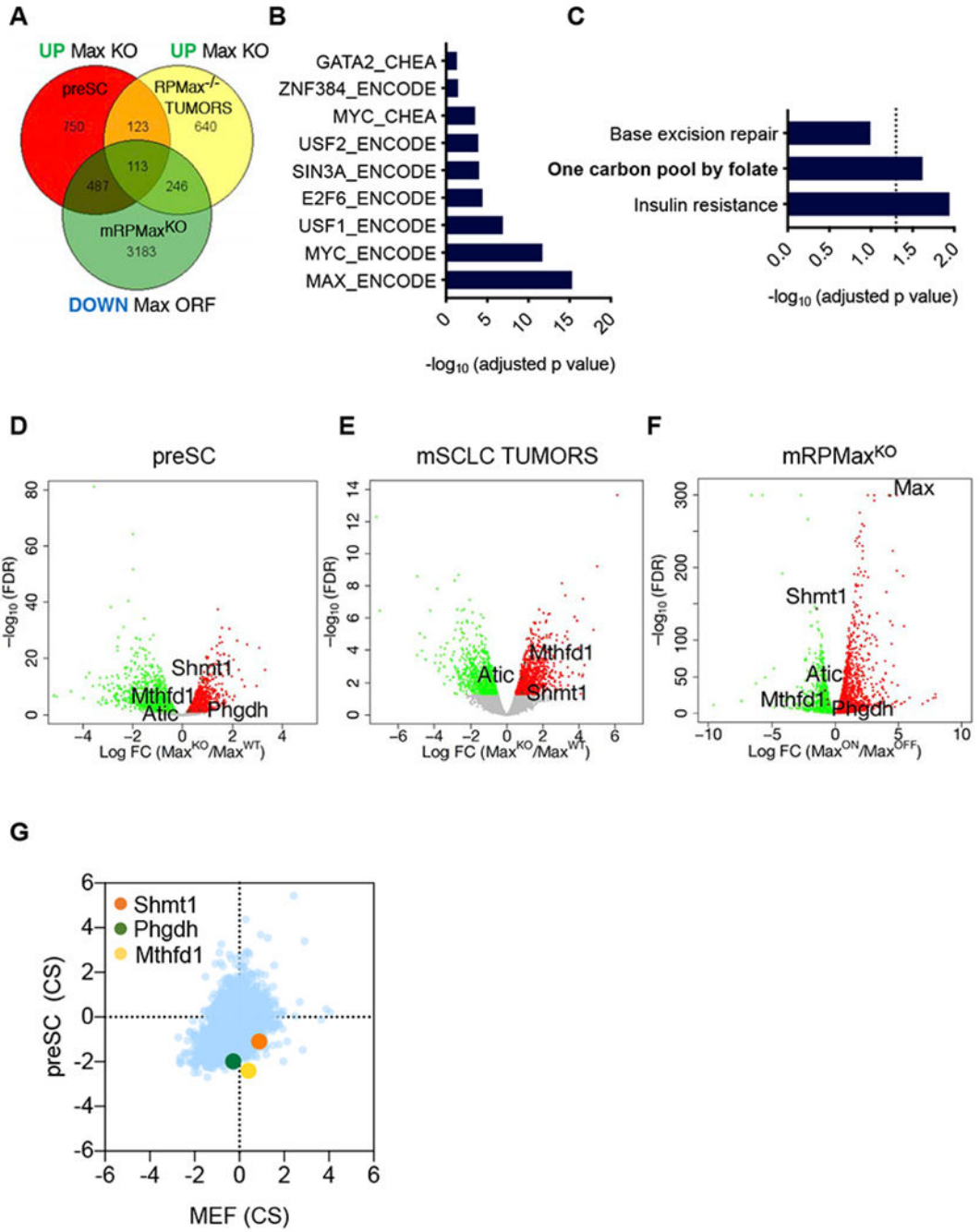


Figure 5. Transcriptional analyses of MAX altered SCLCs

A, Venn diagram of the upregulated genes upon *Max* loss in preSCs and mSCLCs tumors and downregulated upon *Max* restoration in the mRPMMax^{KO} *Max*-null mSCLC line. The list of genes used to generate the Venn diagram were selected from EdgeR analysis with a cut off of FDR<0.05. **B**, ENCODE or CHEA binding analysis for the 113 significant genes from (**A**) shared across the 3 models, upregulated upon *Max* loss and downregulated upon *Max* restoration. An adjusted p value of p<0.05 was considered significant. **C**, KEGG pathway analysis for the 113 genes from (**A**) shared across the 3 models, upregulated upon *Max* loss

and downregulated upon *Max* restoration. An adjusted p value of $p < 0.05$ was considered significant. **D-F**, Volcano plots from the *Max*-KO vs *Max*-WT preSC cell comparison (**D**), *Max* deleted vs *Max* control mSCLC tumors (**E**) and inducible MAX restoration in mRPM^{KO} cell line (**F**) are shown. Significant genes upregulated upon *Max* perturbation are in red or downregulated in green. An FDR < 0.05 was considered significant. Individual genes of interest are depicted. **G**, CRISPR score plot of the metabolic hits of interest showing increased depletion of guide RNAs targeting these genes in preSCs as compared to MEFs following 12 population doublings. See also Figure S5.

Author Manuscript

Author Manuscript

Author Manuscript

Author Manuscript

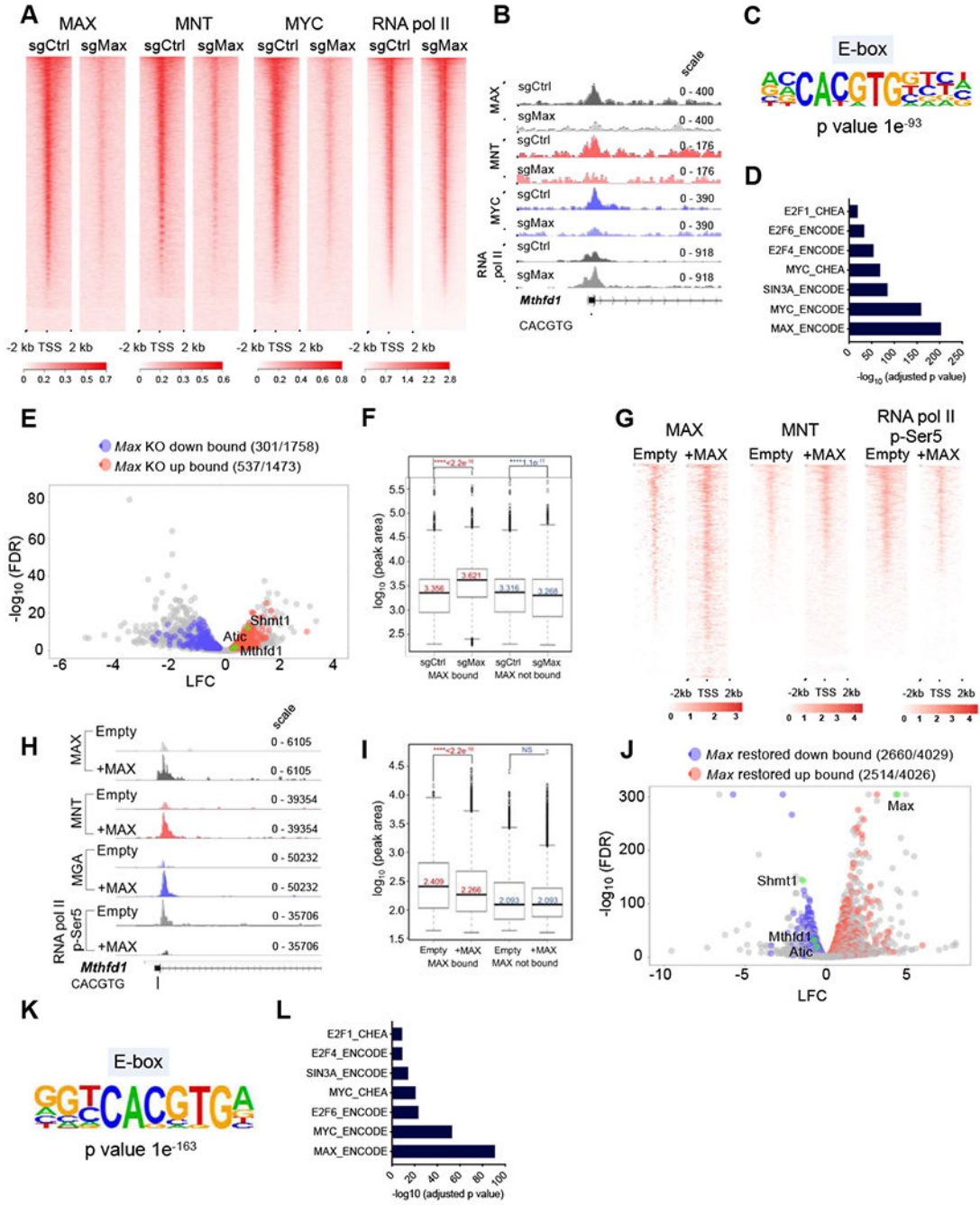


Figure 6. Genomic occupancy of MAX altered SCLC

A, Heat maps depicting promoter enrichment (± 2 kb of TSS) of MAX, MNT, MYC and RNA pol II in control and *Max*-deleted preSCs. **B**, Representative tracks for MAX, MNT, MYC and pol II binding at the *Mthfd1* promoter in preSCs. **C**, Enriched de novo motifs from HOMER analysis on MAX-bound sequences in preSCs. **D**, ENCODE and CHEA analysis on MAX-bound genes in preSCs. **E**, Volcano plot depicting overlap between expression and genomic occupancy analyses (one carbon genes highlighted in green). **F**, Box plots of RNA pol II occupancy at TSS ± 2 kb at MAX bound vs. non-bound genes in *Max*-

null and control preSCs. Box boundaries indicate 1st and 3rd quartiles, whiskers represent 1.5 times the interquartile range, and dots indicate datapoints that fall outside that region. Genes considered MAX-bound if peak occurred -5 kb to TSS. p values computed using Wilcoxon test ($p < 0.01$ considered significant). **G**, Heatmap of MAX, MNT and RNA pol II phospho-Ser5 binding in *Max*-null and MAX restored mRPM^{KO} SCLC cells. **H**, Representative peaks for MAX, MNT, MGA and pol II phospho-Ser5 binding at the *Mthfd1* promoter in mRPM^{KO} SCLC cells. **I**, Box plots depicting RNA pol II phospho-Ser5 occupancy levels at MAX bound vs. unbound genes in MAX restored and *Max*-null mRPM^{KO} SCLC cells. Box boundaries mark 1st and 3rd quartiles, whiskers indicate 1.5 times the interquartile range, and dots represent data points that fall outside that region. Genes considered MAX-bound if peak occurs at TSS to -5 kb. p values computed using Wilcoxon test. **J**, Volcano plot showing overlap between expression and CUT&RUN analyses in MAX restored mRPM^{KO} cells (one carbon genes and *Max* highlighted in green). **K**, HOMER analysis showing significant *de novo* motifs identified from MAX bound sequences in mRPM^{KO} SCLC cells. **L**, ENCODE and CHEA analysis on MAX bound genes in MAX restored mRPM^{KO} cells. See also Figure S6.

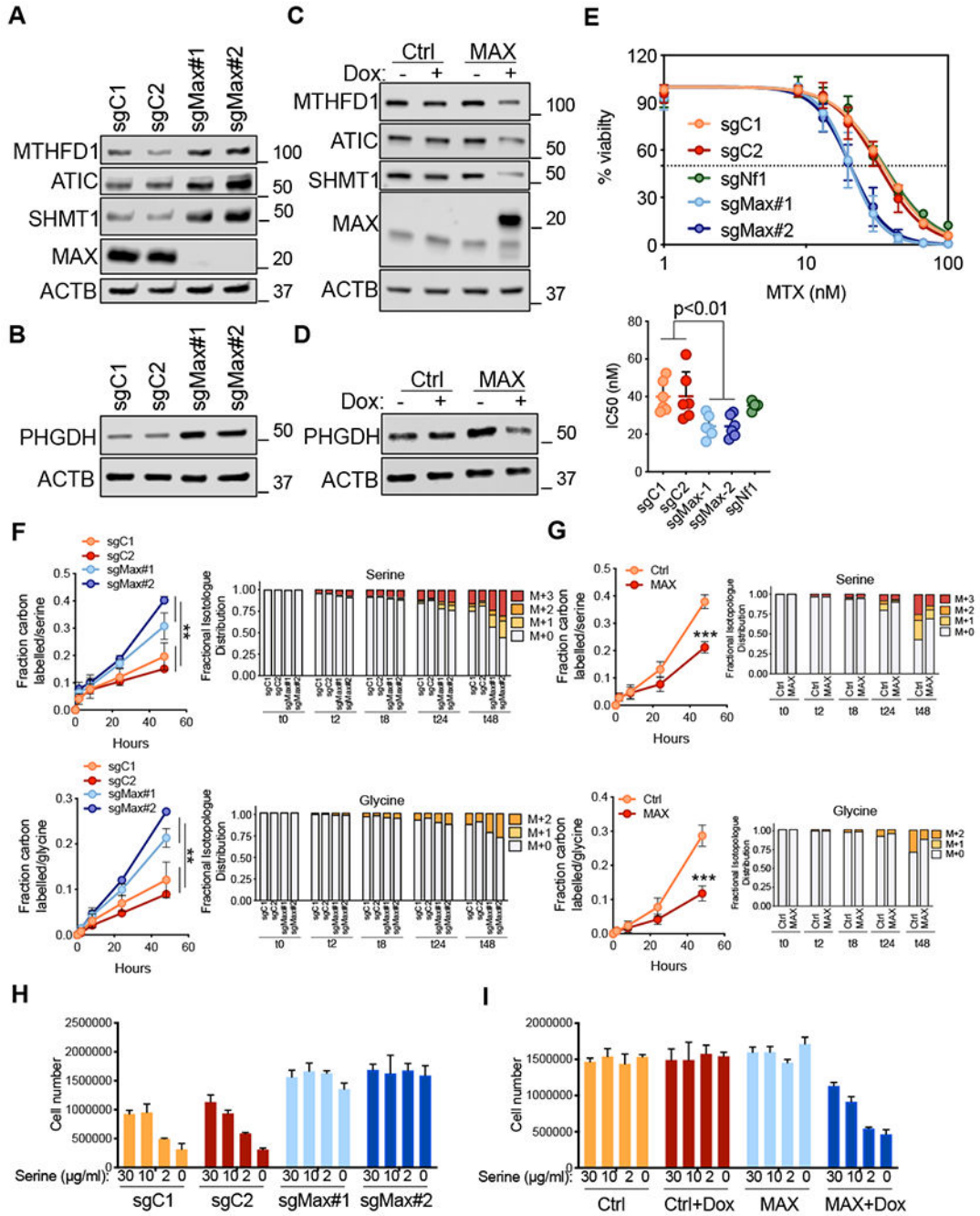


Figure 7. Max deletion results in increased serine and one carbon metabolism

A and **B**, Immunoblotting for MTHFD1, SHMT1, ATIC (**A**) and PHGDH (**B**) proteins upon *Max* loss in preSCs. ACTB was used as a loading control. **C** and **D**, Immunoblotting for MTHFD1, SHMT1, ATIC (**C**) and PHGDH (**D**) upon MAX restoration in mRPMax^{KO} cells. ACTB was used as a loading control. **E**, Dose-response curves of preSCs treated with methotrexate for 96 h. Viability was assessed with the CellTiter-Glo assay and calculated relative to the vehicle control. Data are mean ± SEM from at least n = 3 biological replicates. IC50s are shown for each genotype and each single data point represents an

independent experiment. ** $p < 0.01$, unpaired student's t-test. **F**, U-¹³C glucose tracing experiments in preSCs upon *Max* loss followed across the indicated time points. Fraction carbon labelled and isotopologues for both serine and glycine are shown. ** $p < 0.01$, unpaired student's t-test. **G**, U-¹³C glucose tracing experiments in mRPM^{KO} cell upon MAX restoration followed across the indicated time points. Fraction carbon labelled and isotopologues for both serine and glycine are shown. *** $p < 0.001$, unpaired student's t-test. **H-I**, Growth in serine depleted media for preSCs upon *Max* loss (**H**) and for mRPM^{KO} upon MAX restoration (**I**). Error bars represent mean \pm SD (n=3). See also Figure S7.

Author Manuscript

Author Manuscript

Author Manuscript

Author Manuscript

KEY RESOURCES TABLE

REAGENT or RESOURCE	SOURCE	IDENTIFIER
Antibodies		
JUN	Cell Signaling	9165; RRID: AB_2130165
PTEN	Cell Signaling	9188; RRID: AB_2253290
BAX	Cell Signaling	2772; RRID: AB_10695870
TSC1	Cell Signaling	6935; RRID: AB_10860420
TSC2	Cell Signaling	4308; RRID: AB_10547134
NF1	Bethyl Labs	A300-140A-T; RRID: AB_2779035
BIM	Cell Signaling	2933; RRID: AB_1030947
DLK/MAP3K12	GeneTex	GTX124127; RRID: AB_11170703
PHGDH	Bethyl Labs	A304-732A-T; RRID: AB_2782127
ATIC	Bethyl Labs	A304-271A-T; RRID: AB_2781794
SHMT1	Cell Signaling	80715; RRID: AB_2799957
MTHFD1	Bethyl Labs	A305-285A-M; RRID: AB_2631678
MAX	Santa Cruz	sc-197; RRID: AB_2281783
ACTIN	Sigma	A3854; RRID: AB_262011
HSP90	Santa Cruz	sc-13119; RRID: AB_675659
CGRP	Sigma	C8198-.2ML; RRID: AB_259091
MAX	Proteintech	10426-1-AP; RRID: AB_2141660
MNT	Bethyl Labs	A303-627A; RRID: AB_11205638
MYC	Cell Signaling	13987; RRID: AB_2631168
MYC	Cell Signaling	5605; RRID: AB_1903938
RNApol II	Active Motif	39097; RRID: AB_2732926
RNA pol II phospho Ser5	Cell Signaling	13523; RRID: AB_2799721
MGA	Suske Lab	Stielow et al., 2018
TP53	Cell Signaling	2524; RRID: AB_331743
RB1	Abcam	[EPR17512]; ab181616
GFP	Cell Signaling	2956S; RRID: AB_1196615
MYCL1	R&D SYSTEMS	AF4050; RRID: AB_2282440
Bacterial and Virus Strains		
Ad5-CMV-Cre	University of Iowa Gene Vector Core	VVC-U of Iowa-5;RRID: SCR_015417
Ad5-CGRP-Cre	University of Iowa Gene Vector Core	VVC-Berns-1160 ;RRID: SCR_015417
Chemicals, Peptides, and Recombinant Proteins		
NBF (10 %)	ThermoFisherScientific	5701TS
Trypsin/EDTA (0.05 %)	ThermoFisherScientific	25300054
DMEM	ThermoFisherScientific	11965-092
Puromycin	ThermoFisherScientific	A1113803
Proteinase K	Qiagen	19131

REAGENT or RESOURCE	SOURCE	IDENTIFIER
RNase A	Qiagen	19101
Ammonium acetate/dH2O	Sigma	A1542
TE buffer	Sigma	T9285
RPMI 1640	ThermoFisherScientific	11875-093
Penicillin/ streptomycin	ThermoFisherScientific	15140122
Fetal bovine serum	Omega Scientific	FB-01
Methotrexate	Cayman chemical	13960
Doxycycline	Sigma	44577
Lipofectamine 2000	ThermoFisherScientific	11668019
Hexadimethrine bromide	Sigma	H9268
Crystal violet	Sigma	3886
DAPI	ThermoFisherScientific	P36935
Paraformaldehyde	Fisher	AA433689M
Blasticidin	Invivogen	ant-bl-05
Phusion® High-Fidelity PCR Kit	New England Biolabs	E0553
Trizol	ThermoFisherScientific	15596018
Protease and phosphatase inhibitors	ThermoFisherScientific	78441
4–20 % Mini-PROTEAN®TGX™ Precast Protein Gels	BioRad	4561096
Amersham Protran 0.45 NC nitrocellulose membranes	GE healthcare life science	10600002
Glucose, Glycine and Serine free RPMI	TEKNOVA	R9660-02
Dialyzed serum	ThermoFisherScientific	26400044
Glycine	Sigma	G5417-100G
L-Serine	Sigma	S4311-25G
D-Glucose (U-13C6, 99 %)	Cambridge Isotope Laboratories	CLM-1396-PK
D-(+)-Glucose	Sigma	G7021-100G
Methanol HPLC grade	Sigma	34860
RPMI 1640 2X	Wisent Bioproducts	350-200-CL
SeaPlaque™ Agarose	ThermoFisherScientific	50101
Critical Commercial Assays		
Nanodrop 2000	ThermoFisherScientific	N/A
PureLink quick gel extraction	Invitrogen	K210012
Kapabiosystems Library Quantification Kit	Roche	KK4824
HiSeq 2500	Illumina	N/A
Phusion Flash High Fidelity Master Mix	ThermoFisherScientific	F548L
AgileGrinder™ Tissue Grinder	Thomas Scientific-ACTGene	ACT-AG3080
Ultra RNA Library Prep Kit for Illumina	New England BioLabs	E7530L
NEB Ultra II kit	New England BioLabs	E7645S
Pierce™ BCA Protein Assay Kit	ThermoFisherScientific	23227
CellTiter-Glo assay	Promega	G7573

REAGENT or RESOURCE	SOURCE	IDENTIFIER
Z2 Series Coulter Counter	Beckman Coulter	6605700
iScript reverse transcription supermix for RT-qPCR	Bio-rad	1708840
all-in-One qPCR mix	GeneCopoeia	AOPR-4000
CFX384 Touch Real-Time PCR Detection System	Bio-rad	N/A
Deposited Data		
RNA seq	This paper	Accession Number GEO: GSE138955
CHIP-seq	This paper	Accession Number GEO: GSE146385
CUT&RUN	This paper	Accession Number GEO: GSE146388
Experimental Models: Cell Lines		
Human: 293TN	System Bioscience	LV900A-1
Mouse: preSCs	Kim et al., 2016	N/A
Mouse: mRPM ^{Max} KO	This paper	N/A
Mouse: <i>Trp53</i> ^{lox/lox} MEFs	This paper	N/A
Experimental Models: Organisms/Strains		
<i>Rb</i> ^{fllox/lox} GEMM	Sage et al., 2003	N/A
<i>Trp53</i> ^{lox/lox} GEMM	Meuwissen et al., 2003	N/A
frt-invCAGMyc1 1 -Luc GEMM	Huijbers et al., 2014	N/A
<i>Max</i> ^{lox/lox} GEMM	Mathsyaraja et al., 2019	N/A
Oligonucleotides		
See Table S3	N/A	N/A
Recombinant DNA		
V2 GeCKO mouse library	Sanjana et al., 2014	Addgene; Cat# 1000000052
psPAX2	Gift from Didier Trono	Addgene; Cat# 12260
pMD2.G	Gift from Didier Trono	Addgene; Cat# 12259
pLX304	Yang et al., 2011	Addgene; Cat# 25890
pLX304-MYC	This paper	N/A
pLX304-MYCN	This paper	N/A
pLX304-MYCL	This paper	N/A
pCW 5 7 -RFP-P2A-MC S	Barger et al., 2019	Addgene; Cat# 78933
pCW57-MAX	This paper	N/A
lentiCRISPR v2	Sanjana et al., 2014	Addgene; Cat# 52961
lentiCRISPR v2-sgCtrl# 1	This paper	N/A
lentiCRISPR v2-sgCtrl#2	This paper	N/A
lentiCRISPR v2-sgMax# 1	This paper	N/A
lentiCRISPR v2-sgMax#2	This paper	N/A
lentiCRISPR v2-sgBcl2l1#1	This paper	N/A
lentiCRISPR v2-sgBcl2l1#2	This paper	N/A
lentiCRISPR v2-sgTsc 1 # 1	This paper	N/A
lentiCRISPR v2-sgTsc1#2	This paper	N/A

REAGENT or RESOURCE	SOURCE	IDENTIFIER
lentiCRISPR v2-sgPten# 1	This paper	N/A
lentiCRISPR v2-sgPten#2	This paper	N/A
lentiCRISPR v2-sgMap3k12#1	This paper	N/A
lentiCRISPR v2-sg Map3k12#2	This paper	N/A
lentiCRISPR v2-sgJun#1	This paper	N/A
lentiCRISPR v2-sgJun#2	This paper	N/A
lentiCRISPR v2-sgTsc2# 1	This paper	N/A
lentiCRISPR v2-sgTsc2#2	This paper	N/A
lentiCRISPR v2-sgNf1#1	This paper	N/A
lentiCRISPR v2-sgNf1#2	This paper	N/A
lentiCRISPR v2-sgBax# 1	This paper	N/A
lentiCRISPR v2-sgBax#2	This paper	N/A
lentiCRISPR v2-sgRb1#1	This paper	N/A
lentiCRISPR v2-sgRb1#2	This paper	N/A
lentiCRISPR v2-sgRb12	This paper	N/A
Software and Algorithms		
GraphPad Prism 7	GraphPad Software Inc.	http://www.graphpad.com
ImageStudio Light	ImageStudio Software	https://www.licor.com/bio/image-studio-lite/
Fiji NIH	ImageJ	https://imagej.nih.gov/ij/docs/guide/146-2.html
FlowJo	FlowJo Software	https://www.flowjo.com/
BioRender	BioRender Software	https://biorender.com/
Tracefinder4.1	Tracefinder Software	N/A
ClustVis	Metsalu et al.; 2016	https://bit.cs.ut.ee/clustvis/
MAGeCK-VISPR	MAGeCK-VISPR Software	http://bitbucket.org/liulab/mageck-vispr
TopHat v2.0.12	Trapnell et al., 2009	N/A
Cuffdiff v2.1.1	Trapnell et al., 2013	N/A
Python package HTSeq v0.6.1	Anders et al., 2015	N/A
Bioconductor package edgeR, v3.16	Robinson et al., 2010	N/A
STAR v2.5.2a	Dobin et al., 2013	N/A
Subread package v1.6.0	Liao et al., 2014	N/A